isvr Institute of Sound and Vibration Research

Modelling Ground Vibration from Rail Traffic using the Discrete Wavenumber Finite and Boundary Element Methods

X. Sheng, C.J.C. Jones and D.J. Thompson

ISVR Technical Memorandum No 899

November 2002

University of Southampton

SCIENTIFIC PUBLICATIONS BY THE ISVR

Technical Reports are published to promote timely dissemination of research results by ISVR personnel. This medium permits more detailed presentation than is usually acceptable for scientific journals. Responsibility for both the content and any opinions expressed rests entirely with the author(s).

Technical Memoranda are produced to enable the early or preliminary release of information by ISVR personnel where such release is deemed to the appropriate. Information contained in these memoranda may be incomplete, or form part of a continuing programme; this should be borne in mind when using or quoting from these documents.

Contract Reports are produced to record the results of scientific work carried out for sponsors, under contract. The ISVR treats these reports as confidential to sponsors and does not make them available for general circulation. Individual sponsors may, however, authorize subsequent release of the material.

UNIVERSITY OF SOUTHAMPTON

INSTITUTE OF SOUND AND VIBRATION RESEARCH

DYNAMICS GROUP

Modelling Ground Vibration from Rail Traffic using the Discrete Wavenumber Finite and Boundary Element Methods

by

X. Sheng, C.J.C. Jones and D.J. Thompson

ISVR Technical Memorandum No: 899

November 2002

Authorised for issue by
Professor M.J. Brennan
Group Chairman

CONTENTS

1. INTRODUCTION

An important issue with regard to the environmental impact of rail traffic is the problem of ground vibration produced by trains running on the ground surface or in tunnels. The frequency associated with this problem ranges from 4 Hz to 200 Hz [Grootenhuis 1977]. For trains running on the surface of a ground consisting of layers with horizontally parallel interfaces, the semi-analytical wavenumber-frequency approach can be used [Sheng 2001]. If the ground has arbitrary geometry or if it has some inclusions (i.e. a tunnel) then numerical approaches must be employed. Two numerical approaches are used most commonly, one is the finite element method (FEM) [e.g. Petyt 1990], and the other is the boundary element method (BEM) [e.g. Dominguez 1993].

It is important to model travelling wave behaviour. For this the ground must be modelled as an infinite medium. However, using FEM an artificial boundary must be introduced and only part of the ground is discretised. The artificial boundarie of the ground must incorporate the travelling wave propagation of an infinite medium. In other words, proper boundary conditions, often termed 'transmitting boundary conditions', for the artificial boundary must be introduced in order to ensure that no wave of significant amplitude is reflected. With such boundary conditions applied, the vibration levels due to applied point (nodal) forces can be calculated. The difficulty in using FEM is that, for a three-dimensional problem of large size there is a large number of elements involved in the analysis. Whereas infinite elements have been developed for two-dimensional problems in elasto-dynamics, they have not been well developed for three-dimensional problems with moving sources.

The BEM is very well suited to the analysis of the dynamics of infinite media. Boundless regions are naturally represented. The radiation of waves towards infinity is automatically included in a BEM model which is based on an integral representation valid for internal or external regions. However, BEM is not optimal for thin structures such as tunnels since both faces of a structure have to be discretized, and BEM has numerical problems for thin domains. Therefore for the dynamics of soil-structure interaction, a combination of FEM and BEM appears logically in which the finite structure is modelled using FEM and the ground is modelled using BEM.

A three-dimensional FE/BE model has been implemented [Andersen and Jones 2001 a, b] for the study of train-induced ground vibration. Normally this model is very complicated to use and, because of the extremely large computing resources that are required, cannot be run many times in order to carry out an investigative study for the whole frequency range of interest for structure-borne noise from tunnels. The three-dimensional FE/BE model is useful for many foundation problems where the structure is of limited extent and in which the response of the ground is not required at great distances.

In general situations, the geometry of the ground-tunnel structure is invariant with respect to any translation along the tunnel axis. This feature is also kept for many vibration mitigation devices, such as ditches and wave impedance blocks (WIBs) [Takemiya and Yuasa 1999]. For such structures, an approach was recommended by, for example, Aubry [Aubry et al 1994] in which the problem is transformed into a sequence of two-dimensional models depending on wavenumbers in the tunnel direction. For each longitudinal (tunnel direction) wavenumber, the finite cross-section of the tunnel lining is modelled using the FE method and the wave propagation in the surrounding soil is modelled using the BE method. The actual response of the structure is constructed from that at each wavenumber using an inverse Fourier transform algorithm. The simplicity of this approach comes from the fact that the discretization is only made over the cross-section of the ground-tunnel structure, and therefore the total number of degrees of freedom is greatly reduced compared to the corresponding three-dimensional model. Therefore the memory requirement of this approach is low. Usually calculations are performed for a number of discrete values of wavenumber, which may take a long time if this number is large. However this might be overcome by performing calculations for a few propagating wavenumbers which are dominant over any other wavenumbers.

In addition to tracks and tunnel linings, there are many other built structures which have a constant cross-section and a large length, e.g., water pipes and stiffened plates used in vehicles and long bridge decks. Dynamically, such a structure behaves as a one-dimensional wave guide. The dynamic properties of a waveguide are described by its dispersion curves and mode shapes of the cross-section. In some simple cases, the dispersion curves can be evaluated by using one of the simplified theories (e.g., Euler-Bernoulli and Timoshenko beam theory, the thin shell theory, etc.). However, when the cross-section possesses a complex shape, or when the excitation frequency is high, such simplified theories are not applicable. In this case, two different numerical techniques

based on finite element discretization may be used for numerical computation of the dispersion curves and mode shapes. The first one, presented in reference [Thompson 1993] has been used to compute the dispersion properties of a rail. This method is based on the work of Mead [1973] concerning periodic structures. The length of the periodic structure element is required to be small enough so that waves of short wavelength can be considered. However, too small a length of element would produce computational difficulty. The second one was first proposed by Gavric [Gavric 1994, 1995] for computing the dispersion curves of thin-walled waveguides and free rails. This method is based on factorization of the function describing the displacement field. A finite element discretization is made over the cross-section for each wavenumber in the longitudinal direction. Since, in actual applications, calculations are performed only at a series of discrete wavenumbers, this method may be called *the discrete wavenumber finite element method.* Recently, Shah et al [Shah, Zhuang, Popplewell and Rogers 2001] employed this method to analyse the wave propagation property of thin-walled structural members using in-plane and out-of-plane plate elements.

In the application of BEM to the study of ground vibration, the Green's functions play a key role. The Green's functions are defined as displacements (or other quantities) of an elastic body due to a single unit concentrated load. The Green's functions are available for a homogenous full-space for stationary harmonic sources [Eason, Fulton and Sneddon 1956] and for a layered half-space for both stationary and moving harmonic sources [Sheng, Jones and Petyt 1999]. Here the Green's functions for a whole-space, expressed as a function of two Cartesian coordinates and a wavenumber in the third (axial) dimension are required. These Green's functions, sometime called 'two-and-half-dimensional Green's functions', have also been derived for moving harmonic sources [Sheng, Jones and Thompson 2002] and for stationary harmonic sources [Tadeu and Kausel 2000]. If the Green's functions of a homogenous full-space are employed, then not only the interface of the ground and the built structure, but also the ground surface and the interfaces of the layers must be discretised. In other words, only part of the ground surface and interfaces is taken into account, thus introducing artificial boundaries. However, since the Green's functions for a full-space are formulated in a closed form, they are efficient to use. If the layered half-space Green's functions were employed, then for a ground consisting of parallel layers, only the interface of the ground and the built structure would need to be discretised. However, the Green's functions for a layered half-

space are expressed in terms of boundless integrals, the evaluation of which is time consuming.

In Section 2, the discrete wavenumber finite element formulation is derived for a finite length of a structure using the second Lagrange's equation. It seems to be more rigorous to apply the Lagrange's equation or the Hamiltonian principle to a finite domain than to an infinite domain. The development of the discrete wavenumber boundary element method is presented in Section 3, including the two-and-half dimensional reciprocal theorem in elastodynamics, the Fourier transformed moving Green's functions for a homogeneous whole-space, the discretization of the integral equation over the boundary and the evaluation of singular integral terms. The coupling between a finite element domain and a boundary element domain or between multiple boundary element domains is dealt with in Section 4.

2. DISCRETE WAVENUMBER FINITE ELEMENT METHOD

2.1 DIFFERENTIAL EQUATIONS OF MOTION OF AN ELEMENT

Suppose an elastic body is infinitely long in the x-direction and its cross-sections normal to the x-axis are invariant with x. The x cross-section, A, is discretized into a number of small elements. The same discretization is also made on the $x + dx$ cross-section. An element area, dA, on the x cross-section and its counterpart on the $x + dx$ cross-section define an element prism. The displacements of the nodes of the element dA are denoted by a $3n$ vector

$$\{q(x,t)\} = (u_1, v_1, w_1, u_2, v_2, w_2, \cdots, u_n, v_n, w_n)^T \tag{2.1}$$

where, n is the number of the nodes on the element. The corresponding node force vector is denoted by $\{F(x,t)\}$. A shape function matrix of order $3 \times 3n$ is defined and denoted by $[\Phi(y,z)]$, so that the displacements of the element at any point (x, y, z) may be approximated as

$$\{u(x,y,z,t)\} = (u(x,y,z,t), v(x,y,z,t), w(x,y,z,t))^T = [\Phi(y,z)]\{q(x,t)\} \tag{2.2}$$

The kinetic energy of the element prism (its length is dx) is given by

$$
\begin{aligned}
T &= \frac{1}{2}\int_A \rho\{\dot{u}(x,y,z,t)\}^T\{\dot{u}(x,y,z,t)\}dAdx \\
&= \frac{1}{2}\{\dot{q}(x,t)\}^T\int_A \rho[\Phi(y,z)]^T[\Phi(y,z)]dA\{\dot{q}(x,t)\}dx \\
&= \frac{1}{2}\{\dot{q}(x,t)\}^T[M]\{\dot{q}(x,t)\}dx
\end{aligned}
\tag{2.3}
$$

where, ρ is the density of the material and

$$
[M] = \int_A \rho[\Phi(y,z)]^T[\Phi(y,z)]dA \tag{2.4}
$$

is the mass matrix of the element, which is independent of x.

The potential energy of the element is given by [Petyt 1990]

$$
U = \frac{1}{2}\int_A \{\varepsilon\}^T[D]\{\varepsilon\}dAdx \tag{2.5}
$$

where,

$$
\{\varepsilon\} = (\frac{\partial u}{\partial x}, \frac{\partial \upsilon}{\partial y}, \frac{\partial w}{\partial z}, \frac{\partial u}{\partial y} + \frac{\partial \upsilon}{\partial x}, \frac{\partial u}{\partial z} + \frac{\partial w}{\partial x}, \frac{\partial \upsilon}{\partial z} + \frac{\partial w}{\partial y})^T \tag{2.6}
$$

$$
[D] = \frac{E}{(1+\nu)(1-2\nu)}\begin{bmatrix}
1-\nu & \nu & \nu & 0 & 0 & 0 \\
\nu & 1-\nu & \nu & 0 & 0 & 0 \\
\nu & \nu & 1-\nu & 0 & 0 & 0 \\
0 & 0 & 0 & \frac{1-2\nu}{2} & 0 & 0 \\
0 & 0 & 0 & 0 & \frac{1-2\nu}{2} & 0 \\
0 & 0 & 0 & 0 & 0 & \frac{1-2\nu}{2}
\end{bmatrix} \tag{2.7}
$$

where, E is Young's modulus of the material and ν is Possion ratio. The strain vector $\{\varepsilon\}$ may be written as

$$
\begin{aligned}
\{\varepsilon\} &= (0, \frac{\partial \upsilon}{\partial y}, \frac{\partial w}{\partial z}, \frac{\partial u}{\partial y}, \frac{\partial u}{\partial z}, \frac{\partial \upsilon}{\partial z} + \frac{\partial w}{\partial y})^T + (\frac{\partial u}{\partial x}, 0, 0, \frac{\partial \upsilon}{\partial x}, \frac{\partial w}{\partial x}, 0)^T \\
&= [B]_1\{u(x,y,z,t)\} + [B]_2\frac{\partial}{\partial x}\{u(x,y,z,t)\}
\end{aligned}
\tag{2.8}
$$

where,

$$[B]_1 = \begin{bmatrix} 0 & 0 & 0 \\ 0 & \frac{\partial}{\partial y} & 0 \\ 0 & 0 & \frac{\partial}{\partial z} \\ \frac{\partial}{\partial y} & 0 & 0 \\ \frac{\partial}{\partial z} & 0 & 0 \\ 0 & \frac{\partial}{\partial z} & \frac{\partial}{\partial y} \end{bmatrix}, \qquad [B]_2 = \begin{bmatrix} 1 & 0 & 0 \\ 0 & 0 & 0 \\ 0 & 0 & 0 \\ 0 & 1 & 0 \\ 0 & 0 & 1 \\ 0 & 0 & 0 \end{bmatrix} \tag{2.9}$$

Thus equation (2.5) becomes

$$\begin{aligned} U &= \frac{1}{2}\int_A ([B]_1\{u\} + [B_2]\frac{\partial}{\partial x}\{u\})^T [D]([B]_1\{u\} + [B]_2\frac{\partial}{\partial x}\{u\})dAdx \\ &= \frac{1}{2}\int_A \Big([B]_1[\Phi(y,z)]\{q(x,t)\} + [B_2][\Phi(y,z)]\{\frac{\partial}{\partial x}q(x,t)\}\Big)^T \cdot \\ &\qquad [D]\Big([B]_1[\Phi(y,z)]\{q(x,t)\} + [B]_2[\Phi(y,z)]\{\frac{\partial}{\partial x}q(x,t)\}\Big)dAdx \\ &= \frac{1}{2}\{q(x,t)\}^T\Big(\int_A ([B]_1[\Phi(y,z)])^T[D][B]_1[\Phi(y,z)]dA\Big)\{q(x,t)\}dx \\ &+ \frac{1}{2}\{q(x,t)\}^T\Big(\int_A ([B]_1[\Phi(y,z)])^T[D][B]_2[\Phi(y,z)]dA\Big)\{\frac{\partial}{\partial x}q(x,t)\}dx \\ &+ \frac{1}{2}\{\frac{\partial}{\partial x}q(x,t)\}^T\Big(\int_A ([B]_2[\Phi(y,z)])^T[D][B]_1[\Phi(y,z)]dA\Big)\{q(x,t)\}dx \\ &+ \frac{1}{2}\{\frac{\partial}{\partial x}q(x,t)\}^T\Big(\int_A ([B]_2[\Phi(y,z)])^T[D][B]_2[\Phi(y,z)]dA\Big)\{\frac{\partial}{\partial x}q(x,t)\}dx \end{aligned} \tag{2.10}$$

Letting

$$[K]_0 = \int_A ([B]_1[\Phi(y,z)])^T[D][B]_1[\Phi(y,z)]dA \tag{2.11}$$

$$[R]_1 = \int_A ([B]_1[\Phi(y,z)])^T[D][B]_2[\Phi(y,z)]dA \tag{2.12}$$

$$[R]_2 = \int_A ([B]_2[\Phi(y,z)])^T[D][B]_2[\Phi(y,z)]dA \tag{2.13}$$

then

$$\begin{aligned} U &= \frac{1}{2}\{q(x,t)\}^T[K]_0\{q(x,t)\}dx + \frac{1}{2}\{q(x,t)\}^T[R]_1\{\frac{\partial}{\partial x}q(x,t)\}dx \\ &+ \frac{1}{2}\{\frac{\partial}{\partial x}q(x,t)\}^T[R]_1^T\{q(x,t)\}dx + \frac{1}{2}\{\frac{\partial}{\partial x}q(x,t)\}^T[R]_2\{\frac{\partial}{\partial x}q(x,t)\}dx \end{aligned} \tag{2.14}$$

The virtual work done by the stresses on the x and $x + dx$ cross-sections of the element prism is given by

$$\begin{aligned}\delta W &= \frac{\partial}{\partial x}\int_A [\sigma_x \delta u + \tau_{xy}\delta v + \tau_{xz}\delta w]dAdx \\ &= \frac{\partial}{\partial x}\int_A \{\delta q(x,t)\}^T [\Phi(y,z)]^T \left(([B]_3 + [B]_4 \frac{\partial}{\partial x})[\Phi(y,z)]\{q(x,t)\right)dAdx\end{aligned} \tag{2.15}$$

where, $\{\delta q(x,t)\}$ represents a virtual displacement vector satisfying $\frac{\partial}{\partial x}\{\delta q(x,t)\} = 0$, and

$$\begin{aligned}[B]_3 &= \frac{E}{(1+\nu)(1-2\nu)}\begin{bmatrix} 0 & \nu\frac{\partial}{\partial y} & \nu\frac{\partial}{\partial z} \\ \frac{1-2\nu}{2}\frac{\partial}{\partial y} & 0 & 0 \\ \frac{1-2\nu}{2}\frac{\partial}{\partial z} & 0 & 0 \end{bmatrix} \\ &= \frac{E}{(1+\nu)(1-2\nu)}\begin{bmatrix} \nu & 0 & 0 \\ 0 & (1-2\nu)/2 & 0 \\ 0 & 0 & (1-2\nu)/2 \end{bmatrix}\begin{bmatrix} 0 & \frac{\partial}{\partial y} & \frac{\partial}{\partial z} \\ \frac{\partial}{\partial y} & 0 & 0 \\ \frac{\partial}{\partial z} & 0 & 0 \end{bmatrix}\end{aligned} \tag{2.16}$$

$$[B]_4 = \frac{E}{(1+\nu)(1-2\nu)}\begin{bmatrix} 1-\nu & 0 & 0 \\ 0 & \frac{1-2\nu}{2} & 0 \\ 0 & 0 & \frac{1-2\nu}{2} \end{bmatrix} \tag{2.17}$$

Thus

$$\begin{aligned}&\delta W = \frac{\partial}{\partial x}\int_A \{\delta q(x,t)\}^T [\Phi(y,z)]^T \left(([B]_3 + [B]_4 \frac{\partial}{\partial x})[\Phi(y,z)]\{q(x,t)\right)dAdx \\ &= \int_A \{\delta q(x,t)\}^T [\Phi(y,z)]^T \left(([B]_3[\Phi(y,z)]\{\frac{\partial}{\partial x}q(x,t)\} + [B]_4[\Phi(y,z)]\{\frac{\partial^2}{\partial x^2}\{q(x,t)\}\right)dAdx \\ &= \{\delta q(x,t)\}^T \int_A [\Phi(y,z)]^T ([B]_3[\Phi(y,z)]\{\frac{\partial}{\partial x}q(x,t)\}dAdx \\ &+ \{\delta q(x,t)\}^T \int_A [\Phi(y,z)]^T ([B]_4[\Phi(y,z)]\{\frac{\partial^2}{\partial x^2}q(x,t)\}dAdx\end{aligned}$$

i.e.

$$\delta W = \{\delta q(x,t)\}^T [R]_3\{\frac{\partial}{\partial x}q(x,t)\}dx + \{\delta q(x,t)\}^T [R]_4\{\frac{\partial^2}{\partial x^2}q(x,t)\}dx \tag{2.18}$$

where,

$$[R]_3 = \int_A [\Phi(y,z)]^T [B]_3[\Phi(y,z)]dA \tag{2.19}$$

$$[R]_4 = \int_A [\Phi(y,z)]^T [B]_4[\Phi(y,z)]dA \tag{2.20}$$

The generalised force vector is therefore given by

$$\{Q(x,t)\} = \{F(x,t)\} + [R]_3\{\frac{\partial}{\partial x} q(x,t)\} + [R]_4\{\frac{\partial^2}{\partial x^2} q(x,t)\} \tag{2.21}$$

Inserting equations (2.3), (2.14) and (2.21) into the second Lagrange's equation

$$\frac{d}{dt}\frac{\partial T}{\partial \dot{q}_j} + \frac{\partial U}{\partial q_j} = Q_j \quad (j = 1,2,\cdots,3n) \tag{2.22}$$

yields the differential equation of motion of the element

$$[M]\{\ddot{q}(x,t)\} + [K]_0\{q(x,t)\} + ([R]_1 - [R]_3)\{\frac{\partial}{\partial x} q(x,t)\} - [R]_4\{\frac{\partial^2}{\partial x^2} q(x,t)\} = \{F(x,t)\} \tag{2.23}$$

which may be written as

$$[M]\{\ddot{q}(x,t)\} + [K]_0\{q(x,t)\} + [K]_1\{\frac{\partial}{\partial x} q(x,t)\} - [K]_2\{\frac{\partial^2}{\partial x^2} q(x,t)\} = \{F(x,t)\} \tag{2.24}$$

where, $[K]_1 = [R]_1 - [R]_3$, $[K]_2 = [R]_4$.

It can be seen from equations (2.4), (2.11), (2.13) and (2.20) that, $[M]$, $[K]_0$ and $[K]_2$ are $3n \times 3n$ symmetric matrices, and $[M]$, $[K]_2$ are positive definite and $[K]_0$ is non-negative. All these matrices, including $[R]_1$ and $[R]_3$, are constant, independent of wavenumber β. It can be shown that

$$[R]_1^T = [R]_3 \tag{2.25}$$

thus $[K]_1$ is an anti-symmetric matrix. In fact,

$$[D][B]_2 = \frac{E}{(1+\nu)(1-2\nu)}\begin{bmatrix} 1-\nu & \nu & \nu & 0 & 0 & 0 \\ \nu & 1-\nu & \nu & 0 & 0 & 0 \\ \nu & \nu & 1-\nu & 0 & 0 & 0 \\ 0 & 0 & 0 & \frac{1-2\nu}{2} & 0 & 0 \\ 0 & 0 & 0 & 0 & \frac{1-2\nu}{2} & 0 \\ 0 & 0 & 0 & 0 & 0 & \frac{1-2\nu}{2} \end{bmatrix}\begin{bmatrix} 1 & 0 & 0 \\ 0 & 0 & 0 \\ 0 & 0 & 0 \\ 0 & 1 & 0 \\ 0 & 0 & 1 \\ 0 & 0 & 0 \end{bmatrix}$$

$$= \frac{E}{(1+\nu)(1-2\nu)}\begin{bmatrix} 1-\nu & 0 & 0 \\ \nu & 0 & 0 \\ \nu & 0 & 0 \\ 0 & \frac{1-2\nu}{2} & 0 \\ 0 & 0 & \frac{1-2\nu}{2} \\ 0 & 0 & 0 \end{bmatrix}$$

$$[B]_1[\Phi] = \begin{bmatrix} 0 & 0 & 0 \\ 0 & \frac{\partial}{\partial y} & 0 \\ 0 & 0 & \frac{\partial}{\partial z} \\ \frac{\partial}{\partial y} & 0 & 0 \\ \frac{\partial}{\partial z} & 0 & 0 \\ 0 & \frac{\partial}{\partial z} & \frac{\partial}{\partial y} \end{bmatrix}\begin{bmatrix} \phi_{11} & \phi_{12} & \cdots & \phi_{1n} \\ \phi_{21} & \phi_{22} & \cdots & \phi_{2n} \\ \phi_{31} & \phi_{32} & \cdots & \phi_{3n} \end{bmatrix} = \begin{bmatrix} 0 & \cdots & 0 \\ \frac{\partial \phi_{21}}{\partial y} & \cdots & \frac{\partial \phi_{2n}}{\partial y} \\ \frac{\partial \phi_{31}}{\partial z} & \cdots & \frac{\partial \phi_{3n}}{\partial z} \\ \frac{\partial \phi_{11}}{\partial y} & \cdots & \frac{\partial \phi_{1n}}{\partial y} \\ \frac{\partial \phi_{11}}{\partial z} & \cdots & \frac{\partial \phi_{1n}}{\partial z} \\ \frac{\partial \phi_{21}}{\partial z} + \frac{\partial \phi_{31}}{\partial y} & \cdots & \frac{\partial \phi_{2n}}{\partial z} + \frac{\partial \phi_{3n}}{\partial y} \end{bmatrix}$$

$$([B]_1[\Phi])^T [D][B]_2[\Phi] = \frac{E}{(1+\nu)(1-2\nu)} \times$$

$$\begin{bmatrix} 0 & \frac{\partial \phi_{21}}{\partial y} & \frac{\partial \phi_{31}}{\partial z} & \frac{\partial \phi_{11}}{\partial y} & \frac{\partial \phi_{11}}{\partial z} & \frac{\partial \phi_{21}}{\partial z} + \frac{\partial \phi_{31}}{\partial y} \\ \vdots & \vdots & \vdots & \vdots & \vdots & \vdots \\ 0 & \frac{\partial \phi_{2n}}{\partial y} & \frac{\partial \phi_{3n}}{\partial z} & \frac{\partial \phi_{1n}}{\partial y} & \frac{\partial \phi_{1n}}{\partial z} & \frac{\partial \phi_{2n}}{\partial z} + \frac{\partial \phi_{3n}}{\partial y} \end{bmatrix}\begin{bmatrix} 1-\nu & 0 & 0 \\ \nu & 0 & 0 \\ \nu & 0 & 0 \\ 0 & \frac{1-2\nu}{2} & 0 \\ 0 & 0 & \frac{1-2\nu}{2} \\ 0 & 0 & 0 \end{bmatrix}[\Phi] \qquad (2.26)$$

$$= \frac{E}{(1+\nu)(1-2\nu)}\begin{bmatrix} \nu(\frac{\partial \phi_{21}}{\partial y} + \frac{\partial \phi_{31}}{\partial z}) & \frac{1-2\nu}{2}\frac{\partial \phi_{11}}{\partial y} & \frac{1-2\nu}{2}\frac{\partial \phi_{11}}{\partial z} \\ \vdots & \vdots & \vdots \\ \nu(\frac{\partial \phi_{2n}}{\partial y} + \frac{\partial \phi_{3n}}{\partial z}) & \frac{1-2\nu}{2}\frac{\partial \phi_{1n}}{\partial y} & \frac{1-2\nu}{2}\frac{\partial \phi_{1n}}{\partial z} \end{bmatrix}[\Phi]$$

$$[\Phi]^T[B]_3[\Phi] = \frac{E}{(1+\nu)(1-2\nu)}[\Phi]^T \begin{bmatrix} 0 & \nu\frac{\partial}{\partial y} & \nu\frac{\partial}{\partial z} \\ \frac{1-2\nu}{2}\frac{\partial}{\partial y} & 0 & 0 \\ \frac{1-2\nu}{2}\frac{\partial}{\partial z} & 0 & 0 \end{bmatrix} \begin{bmatrix} \phi_{11} & \phi_{12} & \cdots & \phi_{1n} \\ \phi_{21} & \phi_{22} & \cdots & \phi_{2n} \\ \phi_{31} & \phi_{32} & \cdots & \phi_{3n} \end{bmatrix}$$

$$= \frac{E}{(1+\nu)(1-2\nu)}[\Phi]^T \begin{bmatrix} \nu(\frac{\partial\phi_{21}}{\partial y}+\frac{\partial\phi_{31}}{\partial z}) & \cdots & \nu(\frac{\partial\phi_{2n}}{\partial y}+\frac{\partial\phi_{3n}}{\partial z}) \\ \frac{1-2\nu}{2}\frac{\partial\phi_{11}}{\partial y} & \cdots & \frac{1-2\nu}{2}\frac{\partial\phi_{1n}}{\partial y} \\ \frac{1-2\nu}{2}\frac{\partial\phi_{11}}{\partial z} & \cdots & \frac{1-2\nu}{2}\frac{\partial\phi_{1n}}{\partial z} \end{bmatrix} \tag{2.27}$$

Equation (2.25) is proved by inserting equations (2.26) and (2.27) into equations (2.12) and (2.19) respectively.

Similarly, it can be shown that $[R]_2 = [R]_4$. It should be noted that the matrices $[K]_0$ and $[M]$ are not equal to the stiffness and mass matrices of the either of the corresponding plane-stress or plane strain dynamic problems.

2.2 GLOBAL FINITE ELEMENT EQUATION AND MODAL ANALYSIS

The conventional finite 'summation' of the element matrices in equation (2.24) is still applicable to obtain the corresponding matrices of the assembled finite element model and thus the global differential equation of motion. This is still represented by equation (2.24). Now by applying the Fourier transforms

$$\bar{f}(\beta) = \int_{-\infty}^{\infty} f(x)e^{-i\beta x}dx, \quad f(x) = \frac{1}{2\pi}\int_{-\infty}^{\infty} \bar{f}(\beta)e^{i\beta x}d\beta \tag{2.28}$$

and letting [Sheng, Jones and Petyt 1999]

$$\bar{f}(\beta,t) = \tilde{f}(\beta)e^{i(\Omega-\beta c)t} \tag{2.29}$$

equation (2.24) becomes

$$-\omega^2[M]\{\tilde{q}(\beta)\} + \left([K]_0 + i\beta[K]_1 + \beta^2[K]_2\right)\{\tilde{q}(\beta)\} = \{\tilde{F}(\beta)\} \tag{2.30}$$

where, it has been assumed that the nodal forces all are harmonic with frequency Ω and moving in the x-direction at speed c. The equivalent frequency ω is given by

$$\omega = \Omega - \beta c \tag{2.31}$$

From equation (2.30) the transformed displacement vector $\{\tilde{q}(\beta)\}$ can be worked out and then the actual displacements may be obtained using a Fourier transform algorithm.

The characteristic equation of the free vibration of a waveguide is obtained by setting $\{\tilde{F}(\beta)\}=0$ in equation (2.30),

$$\left([K]_0+i\beta[K]_1+\beta^2[K]_2-\omega^2[M]\right)\{\tilde{q}(\beta)\}=0 \tag{2.32}$$

For a given frequency ω, equation (2.32) leads to a complex quadratic eigenvalue problem. The number of eigenvalues and corresponding eigenvectors is equal to twice the number of degrees of freedom. The eigenvalues can be real, purely imaginary or complex. It can be seen from equation (2.32) that, due to the anti-symmetry of matrix $[K]_1$, if β is an eigenvalue then both $-\beta$ and $\pm\beta^*$ are as well, where, β^* denotes the conjugate of β. This means that waves can propagate in both the positive x- and negative x-directions. The eigenvectors corresponding to β and β^* are conjugate.

The real eigenvalues are the wavenumbers of propagating waves in the waveguide and a knowledge of them is most important in applications. Eigenvectors associated with a real eigenvalue can be either real or complex.

A complex eigenvector associated with a real eigenvalue β is denoted by $\{A\}+i\{B\}$. From equation (2.32)

$$\left([K]_0+i\beta[K]_1+\beta^2[K]_2-\omega^2[M]\right)(\{A\}+i\{B\})=0$$

which gives

$$\left([K]_0+\beta^2[K]_2-\omega^2[M]\right)\{A\}-\beta[K]_1\{B\}=0$$

$$\beta[K]_1\{A\}+\left([K]_0+\beta^2[K]_2-\omega^2[M]\right)\{B\}=0$$

i.e.

$$\left(\beta^2\begin{bmatrix}[K]_2 & 0\\ 0 & [K]_2\end{bmatrix}+\beta\begin{bmatrix}0 & -[K]_1\\ [K]_1 & 0\end{bmatrix}+\begin{bmatrix}[K]_0 & 0\\ 0 & [K]_0\end{bmatrix}-\omega^2\begin{bmatrix}[M] & 0\\ 0 & [M]\end{bmatrix}\right)\begin{Bmatrix}\{A\}\\ \{B\}\end{Bmatrix}=0 \tag{2.33}$$

Given $\beta\geq 0$, equation (2.33) describes a conventional eigenvalue problem in which, the eigenvalue is ω and the eigenvector is $(\{A\}^T, \{B\}^T)^T$.

Generally, as the frequency increases the number of propagating waves also increases. An evanescent wave at low frequency becomes a propagating wave when the excitation frequency reaches a cut-on frequency. At a cut-on frequency the wavelength is infinite (wavenumber is zero). Thus, at a cut-on frequency ω_0, equation (2.32) becomes

$$\left([K]_0 - \omega_0^2[M]\right)\{\tilde{q}\} = 0 \tag{2.34}$$

This is a conventional linear eigenvalue problem. Since matrix $[K]_0$ is non-negative rather than positive definite, some eigenvalues of equation (2.34) will be zero. They correspond to the 'rigid modes' of the cross-section (the cross-section remains undeformed). The non-zero eigenvalues of equation (2.34) correspond to modes which will deform the cross-section.

2.3 VALIDATION

The solution derived in this section and the corresponding computer program has been validated by calculating responses of a circular cylinder of infinite length subject a harmonic load. The analytical solution for such a cylindrical structure subject to moving harmonic loads has been derived by the present authors [Sheng, Jones and Thompson 2002]. The parameters of the cylinder used here are listed in Table 2.1. They correspond to a typical railway tunnel radius and concrete lining.

TABLE 2.1
Parameters for a circular cylinder

Young's modulus ($\times 10^9$ Nm^{-2})	Possion's ratio	Density (kg/m^3)	Loss factor	Inner radius (m)	Outer radius (m)
37.6	0.15	2400	0.05	3.4	3.6

2.3.1 DISPERSION CURVES OF THE CYLINDER

Since its thickness (0.2 m) is small compared to its average radius (3.5 m), the cylinder may be regarded as a thin shell and the dispersion curves may be evaluated using one of the thin shell theories. Figure 2.1 presents the dispersion curves of the cylinder, of circumferential orders 0 to 8, calculated using the Donnel-Mushta thin shell theory [Leissa 1973].

Two types of propagating waves are clearly shown in Figure 2.1 for circumferential order zero (i.e., the axially symmetric modes). For frequencies lower than

160 Hz, the two dispersion curves are straight lines. The upper straight line represents the torsional waves (a circumferential mode) while the lower straight line (an axial mode) represents the longitudinal waves. These two types of wave have small contributions to radial motions.

For circumferential order m = 1, the waves of the first mode for low frequencies are close to the bending (flexural) waves of the cylinder when it is regarded as a beam. It should be noticed that, the bending mode degenerates to a simple translation and hence zero frequency as the wavenumber decreases to zero whatever the thickness of the shell. However, Figure 2.1 indicates a small cut-on frequency resulting from the thin shell theory approximation.

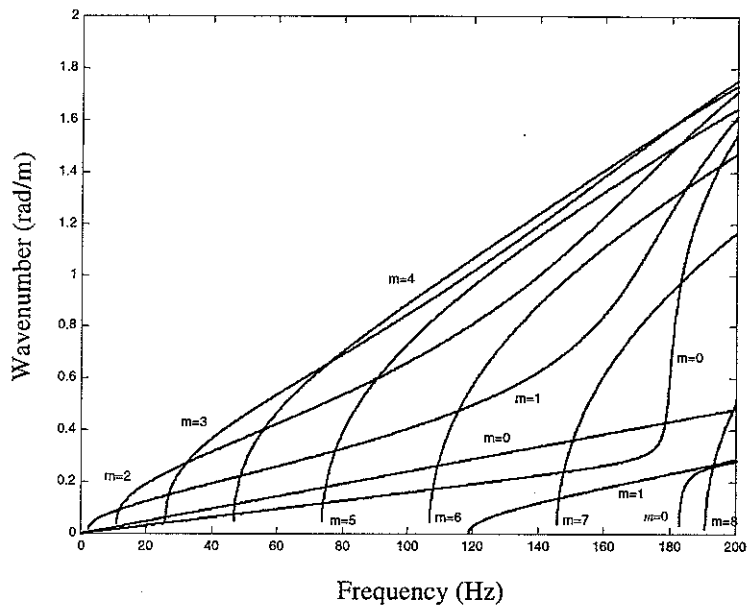

Figure 2.1. Dispersion curves of the cylinder of circumferential orders 0 to 8, calculated using the Donnel-Mushta thin shell theory.

The cut-on frequencies correspond to zero wavenumber. It can be seen from Figure 2.1 that for the tunnel lining, cut-on frequencies in the range up to 200 Hz include the modes up to circumferential order 8. Ground vibration from underground trains typically covers the range from about 20 Hz to 200 Hz.

Figure 2.1 shows that below 200 Hz, the propagating wavenumbers (β) are less than 2 rad/m. In other words, the wavelengths in the axial direction are greater than about 3.14 m. This information is important in the determination of the wavenumber spacing used in the inverse Fourier transform.

2.3.2 DISPLACEMENTS OF THE CYLINDER

Figures 2.2 to 2.4 present comparisons between the FEM solution and the analytic solution. They show the radial displacements along the generator containing the loading point which is on the outer surface of the cylinder. Figures 2.2 and 2.3 are for a unit stationary load of, respectively, 80 Hz and 200 Hz, acting in the radial direction. Figure 2.4 shows the response for the load of 200 Hz moving at 100 m/s in the axial direction. In the finite element mesh, 60 eight-noded quadrilateral elements are employed. The size of each element is 0.2 m in the cylinder thickness direction and 0.37 m in the circumferential direction. In the performance of the inverse FFT, 2048 samples are used with a spacing of β equal to $0.0025\times 2\pi$ (rad/m). These figures indicate that a high computational accuracy of the FEM model has been achieved.

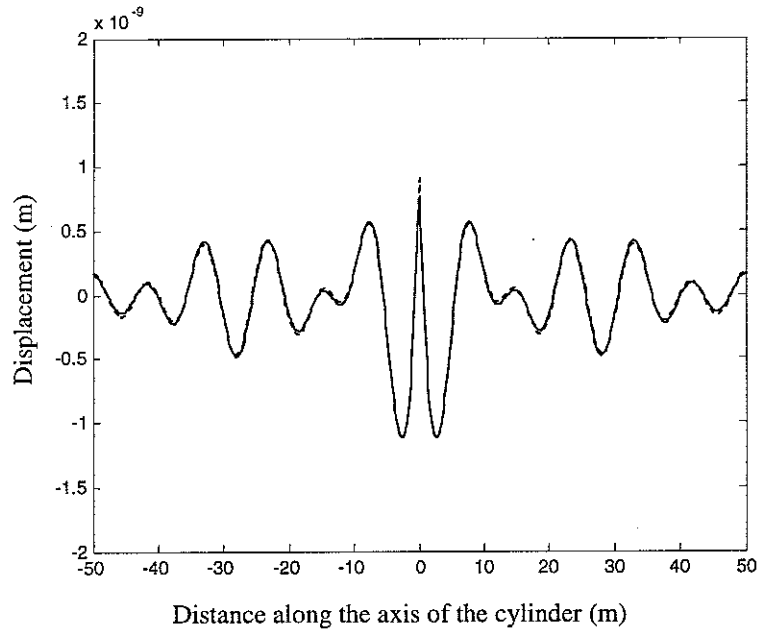

Figure 2.2. Radial displacements of the generator containing the loading point due to a unit radial harmonic load of 80 Hz. ——, from the analytical model; – – –, from the FEM model in which 60 eight-noded quadrilateral elements are used.

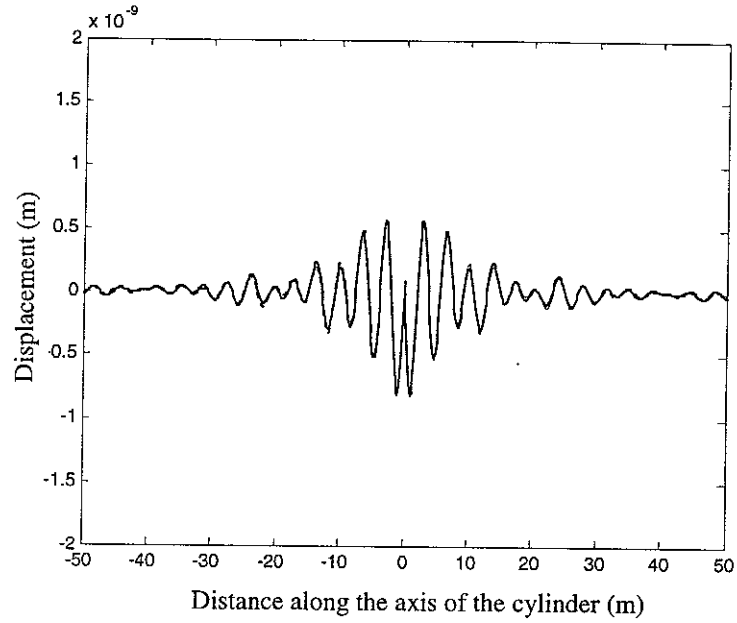

Figure 2.3. Radial displacements of the generator containing the loading point due to a unit radial harmonic load of 200 Hz. ——, from the analytical model; – – –, from the FEM model in which 60 eight-noded quadrilateral elements are used.

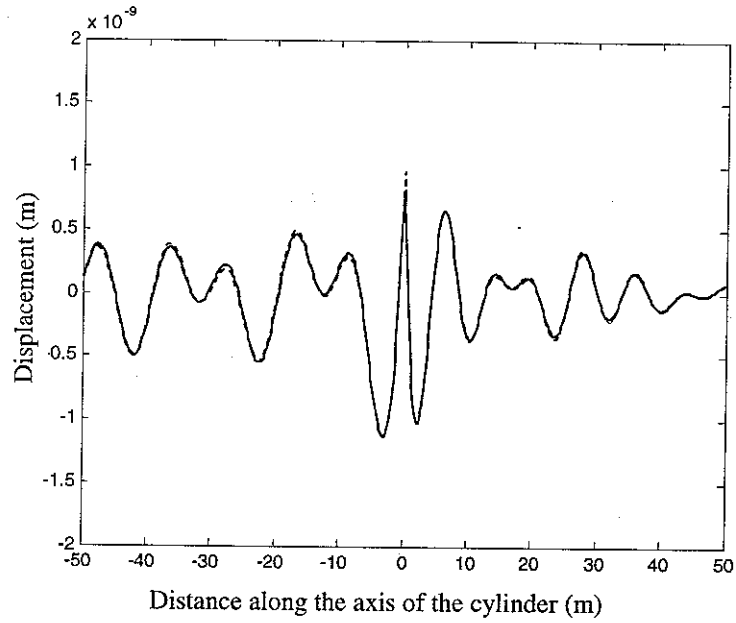

Figure 2.4. Radial displacements of the generator containing the loading point due to a unit radial harmonic load of 80 Hz moving at 100 m/s. ——, from the analytical model; – – –, from the FEM model in which 60 eight-noded quadrilateral elements are used.

3. DISCRETE WAVENUMBER BOUNDARY ELEMENT METHOD

3.1 THE TWO-AND-HALF DIMENSIONAL RECIPROCAL THEOREM IN ELASTODYNAMICS

Suppose an elastic body is infinitely long in the x-direction and its cross-section normal to the x-axis is invariant with x. The cross-section is denoted by A and the boundary of A in its own plane is denoted by Γ. For this elastic body, two elastodynamic states are defined. The first one is described by displacements $u_k(x,y,z,t)$, body forces $\rho b_k(x,y,z,t)$ and boundary tractions $p_k(x,y,z,t)$, where $k = 1, 2, 3$ corresponding to x-, y- and z-directions, and ρ is the density of the elastic body. The second state is described by $u_k^*(x,y,z,t)$, $\rho b_k^*(x,y,z,t)$ and $p_k^*(x,y,z,t)$. A reciprocal relation between these two states exists and is stated as [Dominguez, 1993]

$$\begin{aligned}&\int_\Gamma \int_{-\infty}^{\infty}(p_k * u_k^*)dxd\Gamma + \int_A \int_{-\infty}^{\infty}\rho(b_k * u_k^* + u_{0k}\dot{u}_k^* + v_{0k}u_k^*)dxdA = \\ &\int_\Gamma \int_{-\infty}^{\infty}(p_k^* * u_k)dxd\Gamma + \int_A \int_{-\infty}^{\infty}\rho(b_k^* * u_k + u_{0k}^*\dot{u}_k + v_{0k}^*u_k)dxdA\end{aligned} \tag{3.1}$$

where, the summation convention over the repeated index applies, '$*$' denotes the Riemann convolution which applies only with time t and is defined as

$$g(t) * h(t) = \begin{cases}\int_0^t g(t-\tau)h(\tau)d\tau, & \text{for } t \geq 0 \\ 0, & \text{for } t < 0\end{cases} \tag{3.2}$$

and

$$u_{0k} = u_k(x,y,z,0), \quad \dot{u}_{0k} = \frac{\partial u_k(x,y,z,0)}{\partial t} \tag{3.3}$$

are initial displacements and velocities.

Since the elastic body is infinitely long in the x-direction, the two elastodynamic states can be expressed in terms of the Fourier integral, for instance

$$u_k(x,y,z,t) = \frac{1}{2\pi}\int_{-\infty}^{\infty}\overline{u}_k(\beta,y,z,t)e^{i\beta x}dx \tag{3.4}$$

where,

$$\overline{u}_k(\beta, y, z, t) = \int_{-\infty}^{\infty} u_k(x, y, z, t) e^{-i\beta x} dx \tag{3.5}$$

is the Fourier transform of $u_k(x, y, z, t)$. Inserting equation (3.4) into equation (3.1), gives

$$\begin{aligned}
&\int_{\Gamma}\int_{-\infty}^{\infty}\left(\int_{-\infty}^{\infty}\overline{p}_k e^{i\beta x}d\beta * \int_{-\infty}^{\infty}\overline{u}_k^* e^{i\beta' x}d\beta'\right)dxd\Gamma + \int_A\int_{-\infty}^{\infty}\rho\left(\int_{-\infty}^{\infty}\overline{b}_k e^{i\beta x}d\beta * \int_{-\infty}^{\infty}\overline{u}_k^* e^{i\beta' x}d\beta'\right)dxdA + \\
&\int_A\int_{-\infty}^{\infty}\rho\left(\int_{-\infty}^{\infty}\overline{u}_{0k} e^{i\beta x}d\beta \times \int_{-\infty}^{\infty}\overline{u}_k^* e^{i\beta' x}d\beta'\right)dxdA + \int_A\int_{-\infty}^{\infty}\rho\left(\int_{-\infty}^{\infty}\overline{v}_{0k} e^{i\beta x}d\beta \times \int_{-\infty}^{\infty}\overline{u}_k^* e^{i\beta' x}d\beta'\right)dxdA = \\
&\int_{\Gamma}\int_{-\infty}^{\infty}\left(\int_{-\infty}^{\infty}\overline{p}_k^* e^{i\beta x}d\beta * \int_{-\infty}^{\infty}\overline{u}_k e^{i\beta' x}d\beta'\right)dxd\Gamma + \int_A\int_{-\infty}^{\infty}\rho\left(\int_{-\infty}^{\infty}\overline{b}_k^* e^{i\beta x}d\beta * \int_{-\infty}^{\infty}\overline{u}_k e^{i\beta' x}d\beta'\right)dxdA + \\
&\int_A\int_{-\infty}^{\infty}\rho\left(\int_{-\infty}^{\infty}\overline{u}_{0k}^* e^{i\beta x}d\beta \times \int_{-\infty}^{\infty}\overline{u}_k e^{i\beta' x}d\beta'\right)dxdA + \int_A\int_{-\infty}^{\infty}\rho\left(\int_{-\infty}^{\infty}\overline{v}_{0k}^* e^{i\beta x}d\beta \times \int_{-\infty}^{\infty}\overline{u}_k e^{i\beta' x}d\beta'\right)dxdA
\end{aligned} \tag{3.6}$$

The triple integrals in equation (3.6), e.g. $\int_{-\infty}^{\infty}\left(\int_{-\infty}^{\infty}\overline{p}_k e^{i\beta x}d\beta * \int_{-\infty}^{\infty}\overline{u}_k^* e^{i\beta' x}d\beta'\right)dx$, can be simplified by making use of the fact that $\overline{p}_k$ and $\overline{u}_k^*$ are independent of x, i.e.

$$\int_{-\infty}^{\infty}\left(\int_{-\infty}^{\infty}\overline{p}_k e^{i\beta x}d\beta * \int_{-\infty}^{\infty}\overline{u}_k^* e^{i\beta' x}d\beta'\right)dx = \int_{-\infty}^{\infty}\int_{-\infty}^{\infty}[(\overline{p}_k * \overline{u}_k^*)\int_{-\infty}^{\infty}e^{i(\beta+\beta')x}dx]d\beta d\beta' \tag{3.7}$$

Since $\int_{-\infty}^{\infty}e^{i(\beta+\beta')x}dx = 2\pi\delta(\beta+\beta')$, where, $\delta(\cdot)$ is the Dirac-δ, and $\overline{p}_k = \overline{p}_k(\beta, y, z, t)$, $\overline{u}_k^* = \overline{u}_k^*(\beta', y, z, t)$, then equation (3.7) becomes

$$\begin{aligned}
&\int_{-\infty}^{\infty}\left(\int_{-\infty}^{\infty}\overline{p}_k e^{i\beta x}d\beta * \int_{-\infty}^{\infty}\overline{u}_k^* e^{i\beta' x}d\beta'\right)dx = 2\pi\int_{-\infty}^{\infty}\int_{-\infty}^{\infty}(\overline{p}_k * \overline{u}_k^*)\delta(\beta+\beta')d\beta d\beta' \\
&= 2\pi\int_{-\infty}^{\infty}\left([\overline{p}_k(\beta, y, z, t) * \int_{-\infty}^{\infty}\overline{u}_k^*(\beta', y, z, t)]\delta(\beta+\beta')d\beta'\right)d\beta
\end{aligned}$$

i.e.

$$\int_{-\infty}^{\infty}\left(\int_{-\infty}^{\infty}\overline{p}_k e^{i\beta x}d\beta * \int_{-\infty}^{\infty}\overline{u}_k^* e^{i\beta' x}d\beta'\right)dx = 2\pi\int_{-\infty}^{\infty}[\overline{p}_k(\beta, y, z, t) * \overline{u}_k^*(-\beta, y, z, t)]d\beta \tag{3.8}$$

It can be seen from equation (3.8) that the integral on the right-hand side may also be expressed as

$$\int_{-\infty}^{\infty}[\overline{p}_k(\beta,y,z,t)*\overline{u}_k^*(-\beta,y,z,t)]d\beta=\int_{-\infty}^{\infty}[\overline{p}_k(-\beta,y,z,t)*\overline{u}_k^*(\beta,y,z,t)]d\beta \tag{3.9}$$

By inserting equation (3.8) into the left side of equation (3.6) and equation (3.9) into the right side of equation (3.6), it can be shown that equation (3.6) holds if for every value of β

$$\begin{aligned}&\int_\Gamma[\overline{p}_k(\beta,y,z,t)*\overline{u}_k^*(-\beta,y,z,t)]d\Gamma+\int_A\rho[\overline{b}_k(\beta,y,z,t)*\overline{u}_k^*(-\beta,y,z,t)]dA\\&+\int_A\rho[\overline{u}_{0k}(\beta,y,z)\times\dot{\overline{u}}_k^*(-\beta,y,z,t)]dA+\int_A\rho[\overline{v}_{0k}(\beta,y,z)\times\overline{u}_k^*(-\beta,y,z,t)]dA=\\&\int_\Gamma[\overline{p}_k^*(-\beta,y,z,t)*\overline{u}_k(\beta,y,z,t)]d\Gamma+\int_A\rho[\overline{b}_k^*(-\beta,y,z,t)*\overline{u}_k(\beta,y,z,t)]dA\\&+\int_A\rho[\overline{u}_{0k}^*(-\beta,y,z)\times\dot{\overline{u}}_k(\beta,y,z,t)]dA+\int_A\rho[\overline{v}_{0k}^*(-\beta,y,z)\times\overline{u}_k(\beta,y,z,t)]dA\end{aligned} \tag{3.10}$$

Now it is assumed that the first elastodynamic state is due to harmonic loads of angular frequency Ω moving in the positive x-direction at speed c while the second state is due to harmonic loads of the same frequency but moving *in the negative x-direction at speed c*. Thus, it may be written that [Sheng, Jones and Petyt 1999]

$$\overline{u}_k(\beta,y,z,t)=\tilde{u}_k(\beta,y,z)e^{i(\Omega-\beta c)t}=\tilde{u}_k e^{i(\Omega-\beta c)t} \tag{3.11}$$

$$\overline{p}_k(\beta,y,z,t)=\tilde{p}_k(\beta,y,z)e^{i(\Omega-\beta c)t}=\tilde{p}_k e^{i(\Omega-\beta c)t} \tag{3.12}$$

$$\overline{b}_k(\beta,y,z,t)=\tilde{b}_k(\beta,y,z)e^{i(\Omega-\beta c)t}=\tilde{b}_k e^{i(\Omega-\beta c)t} \tag{3.13}$$

$$\overline{u}_k^*(\beta,y,z,t)=\tilde{u}_k^*(\beta,y,z)e^{i(\Omega+\beta c)t}=\tilde{u}_k^* e^{i(\Omega+\beta c)t} \tag{3.14}$$

$$\overline{p}_k^*(\beta,y,z,t)=\tilde{p}_k^*(\beta,y,z)e^{i(\Omega+\beta c)t}=\tilde{p}_k^* e^{i(\Omega+\beta c)t} \tag{3.15}$$

$$\overline{b}_k^*(\beta,y,z,t)=\tilde{b}_k^*(\beta,y,z)e^{i(\Omega+\beta c)t}=\tilde{b}_k^* e^{i(\Omega+\beta c)t} \tag{3.16}$$

Equations (3.11) and (3.14) imply that

$$\overline{u}_{0k}=\tilde{u}_k,\ \overline{u}_{0k}^*=\tilde{u}_k^*,\ \overline{v}_{0k}=i(\Omega-\beta c)\tilde{u}_k,\ \overline{v}_{0k}^*=i(\Omega+\beta c)\tilde{u}_k^* \tag{3.17}$$

Inserting equations (3.11) to (3.17) into equation (3.10) and performing the convolution defined by equation (3.2), yields

$$
\begin{aligned}
&te^{i(\Omega-\beta c)t}\int_{\Gamma}\tilde{p}_k(\beta,y,z)\tilde{u}_k^*(-\beta,y,z)d\Gamma+te^{i(\Omega-\beta c)t}\int_A\rho\tilde{b}_k(\beta,y,z)\tilde{u}_k^*(-\beta,y,z)dA\\
&+i(\Omega-\beta c)e^{i(\Omega-\beta c)t}\int_A\rho\tilde{u}_k(\beta,y,z)\tilde{u}_k^*(-\beta,y,z)dA+\\
&i(\Omega-\beta c)e^{i(\Omega-\beta c)t}\int_A\rho\tilde{u}_k(\beta,y,z)\tilde{u}_k^*(-\beta,y,z)dA=\\
&te^{i(\Omega-\beta c)t}\int_{\Gamma}\tilde{p}_k^*(-\beta,y,z)\tilde{u}_k(\beta,y,z)d\Gamma+te^{i(\Omega-\beta c)t}\int_A\rho\tilde{b}_k^*(-\beta,y,z)\tilde{u}_k(\beta,y,z)dA\\
&+i(\Omega-\beta c)e^{i(\Omega-\beta c)t}\int_A\rho\tilde{u}_k^*(-\beta,y,z)\tilde{u}_k(\beta,y,z)dA+\\
&i(\Omega-\beta c)e^{i(\Omega-\beta c)t}\int_A\rho\tilde{u}_k^*(-\beta,y,z)\tilde{u}_k(\beta,y,z)dA
\end{aligned}
\tag{3.18}
$$

which leads to

$$
\begin{aligned}
&\int_{\Gamma}\tilde{p}_k(\beta,y,z)\tilde{u}_k^*(-\beta,y,z)d\Gamma+\int_A\rho\tilde{b}_k(\beta,y,z)\tilde{u}_k^*(-\beta,y,z)dA=\\
&\int_{\Gamma}\tilde{p}_k^*(-\beta,y,z)\tilde{u}_k(\beta,y,z)d\Gamma+\int_A\rho\tilde{b}_k^*(-\beta,y,z)\tilde{u}_k(\beta,y,z)dA
\end{aligned}
\tag{3.19}
$$

Equation (3.19) represents the reciprocal relation between the two states in the wavenumber domain, and therefore is termed *the two-and-half dimensional reciprocal theorem* in elastodynamics. Equation (3.19) recovers the reciprocal theorem in elastodynamics for a plane-strain problem when β is set to zero.

Now the displacements and stresses in the second elastodynamic state are assumed to be identical to those of a whole-space (the elastic body is a part of the whole-space) due to a harmonic load of frequency Ω. This load moves at speed c in the negative x-direction along a straight line which passes through (y_0, z_0) and is parallel to the x-axis. Thus the body force for the second state is given by

$$\rho b_k^*(x,y,z,t)=\delta(x+ct)\delta(y-y_0,z-z_0)\delta_{kl}e^{i\Omega t} \tag{3.20}$$

where, δ_{kl} is Kronecker's delta. Fourier transforming equation (3.20) yields

$\rho\bar{b}_k^*=\delta(y-y_0,z-z_0)\delta_{kl}e^{i(\Omega+\beta c)t}$, which, according to equation (3.16), means

$$\rho\tilde{b}_k^*=\delta(y-y_0,z-z_0)\delta_{kl} \tag{3.21}$$

Inserting equation (3.21) into equation (3.19) gives

$$
\begin{aligned}
&\delta_{kl}\tilde{u}_k(\beta, y_0, z_0) \\
&= \int_\Gamma [\tilde{p}_k(\beta, y, z)\tilde{u}^*_{kl}(-\beta, y, z; y_0, z_0) - \tilde{p}^*_{kl}(-\beta, y, z; y_0, z_0)\tilde{u}_k(\beta, y, z)]d\Gamma \\
&+ \int_A \rho\tilde{b}_k(\beta, y, z)\tilde{u}^*_{kl}(-\beta, y, z; y_0, z_0)dA
\end{aligned} \tag{3.22}
$$

Equation (3.22) is an integral equation which associates the displacements at point (y_0, z_0) with the displacements and tractions on the boundary, and the externally applied body forces. In equation (3.22), $\tilde{u}^*_{kl}(-\beta, y, z; y_0, z_0)$ and $\tilde{p}^*_{kl}(-\beta, y, z; y_0, z_0)$ are used to denote the Fourier transformed moving Green's functions (displacement and traction) due to the moving load defined in equation (3.20). The first subscript indicates the response direction while the second denotes the source direction. These Green's functions have been derived by the present authors in [Sheng, Jones and Thompson 2002] and will be presented in the next sub-section. Equation (3.22) may be expressed in matrix form

$$
\begin{aligned}
&\{\tilde{u}(\beta, y_0, z_0)\} \\
&= \int_\Gamma \left([\tilde{U}^*(-\beta, y, z; y_0, z_0)]^T\{\tilde{p}(\beta, y, z)\} - [\tilde{P}^*(-\beta, y, z; y_0, z_0)]^T\{\tilde{u}(\beta, y, z)\}\right)d\Gamma \\
&+ \int_A [\tilde{U}^*(-\beta, y, z; y_0, z_0)]^T\{\rho\tilde{b}(\beta, y, z)\}dA
\end{aligned} \tag{3.23}
$$

where,

$$
\{\tilde{u}\} = (\tilde{u}_1, \tilde{u}_2, \tilde{u}_3)^T \tag{3.24a}
$$

is the displacement vector at (y_0, z_0),

$$
\{\tilde{p}\} = (\tilde{p}_1, \tilde{p}_2, \tilde{p}_3)^T \tag{3.24b}
$$

is the surface traction vector,

$$
[\tilde{U}^*] = \begin{bmatrix} \tilde{u}^*_{11} & \tilde{u}^*_{12} & \tilde{u}^*_{13} \\ \tilde{u}^*_{21} & \tilde{u}^*_{22} & \tilde{u}^*_{23} \\ \tilde{u}^*_{31} & \tilde{u}^*_{32} & \tilde{u}^*_{33} \end{bmatrix} \tag{3.24c}
$$

is the displacement Green's function matrix, and

$$
[\tilde{P}^*] = \begin{bmatrix} \tilde{p}^*_{11} & \tilde{p}^*_{12} & \tilde{p}^*_{13} \\ \tilde{p}^*_{21} & \tilde{p}^*_{22} & \tilde{p}^*_{23} \\ \tilde{p}^*_{31} & \tilde{p}^*_{32} & \tilde{p}^*_{33} \end{bmatrix} \tag{3.24d}
$$

is the traction Green's function matrix.

3.2 THE FOURIER-TRANSFORMED MOVING GREEN'S FUNCTIONS FOR A HOMOGENEOUS WHOLE-SPACE

The integral equation (3.22) or (3.23) requires the Fourier-transformed moving Green's functions for a homogeneous whole-space. These Green's functions due to a unit harmonic load of frequency Ω *acting on the x-axis and moving at speed c in the positive x-direction* are listed and discussed in this sub-section. The detailed derivation can be found in reference [Sheng, Jones and Thompson 2002].

3.2.1 *DISPLACEMENT GREEN'S FUNCTIONS*

The displacement Green's functions are given by

$$\tilde{u}_{11}^{*}(\beta, y, z) = \frac{1}{2\pi\rho\omega^2}[\beta^2 K_0(p_1 r) - p_2^2 K_0(p_2 r)] \tag{3.25a}$$

$$\tilde{u}_{21}^{*}(\beta, y, z) = \tilde{u}_{12}^{*}(\beta, y, z) = \frac{i\beta}{2\pi\rho\omega^2}\frac{y}{r}[p_1 K_1(p_1 r) - p_2 K_1(p_2 r)] \tag{3.25b}$$

$$\tilde{u}_{31}^{*}(\beta, y, z) = \tilde{u}_{13}^{*}(\beta, y, z) = \frac{i\beta}{2\pi\rho\omega^2}\frac{z}{r}[p_1 K_1(p_1 r) - p_2 K_1(p_2 r)] \tag{3.25c}$$

$$\begin{aligned}\tilde{u}_{22}^{*}(\beta, y, z) = \frac{1}{2\pi\rho\omega^2}\{&\frac{y^2}{r^2}[p_2^2 K_2(p_2 r) - p_1^2 K_2(p_1 r)] + \omega^2 K_0(p_2 r)/c_2^2 \\ &+ \frac{p_1}{r}K_1(p_1 r) - \frac{p_2}{r}K_1(p_2 r)\}\end{aligned} \tag{3.25d}$$

$$\tilde{u}_{32}^{*}(\beta, y, z) = \tilde{u}_{23}^{*}(\beta, y, z) = \frac{1}{2\pi\rho\omega^2}\frac{yz}{r^2}[p_2^2 K_2(p_2 r) - p_1^2 K_2(p_1 r)] \tag{3.25e}$$

$$\begin{aligned}\tilde{u}_{33}^{*}(\beta, y, z) = \frac{1}{2\pi\rho\omega^2}\{&\frac{z^2}{r^2}[p_2^2 K_2(p_2 r) - p_1^2 K_2(p_1 r)] + \omega^2 K_0(p_2 r)/c_2^2 \\ &+ \frac{p_1}{r}K_1(p_1 r) - \frac{p_2}{r}K_1(p_2 r)\}\end{aligned} \tag{3.25f}$$

In equations (3.25), $K_n(\cdot)$ ($n = 0, 1, 2$) is the modified Bessel function of order n of the second kind,

$$\omega = \Omega - \beta c \tag{3.26a}$$

$$p_1 = \sqrt{\beta^2 - \frac{\omega^2}{c_1^2}}, \quad p_2 = \sqrt{\beta^2 - \frac{\omega^2}{c_2^2}} \tag{3.26b}$$

are wavenumbers in the yz plane

$$r = \sqrt{y^2 + z^2} \tag{3.26c}$$

c_1 and c_2 are the complex P- and S-wave speeds of the material. Equation (3.25) shows that matrix $[\tilde{U}^*]$, defined by equation (3.24c), is a symmetric matrix.

3.2.2 *ANALYSIS OF THE DISPLACEMENT GREEN'S FUNCTIONS*

3.2.2.1 *Moving harmonic load*

In this case, the load frequency $\Omega \neq 0$ and the load speed $c \neq 0$. There are two special situations that must be identified.

(1) When $\beta = 0$ (therefore $\omega \neq 0$ according to equation (3.26a)), a plane-strain problem results, and equation (3.25) gives the Green's functions for a whole-plane (yz plane):

$$\tilde{u}_{11}^*(0, y, z) = \frac{1}{2\pi\rho c_2^2} K_0(i\frac{\omega r}{c_2}) \tag{3.27a}$$

$$\tilde{u}_{21}^*(0, y, z) = \tilde{u}_{12}^*(0, y, z) = 0 \tag{3.27b}$$

$$\tilde{u}_{31}^*(0, y, z) = \tilde{u}_{13}^*(0, y, z) = 0 \tag{3.27c}$$

$$\begin{aligned}\tilde{u}_{22}^*(0, y, z) = \frac{1}{2\pi\rho}\{&\frac{y^2}{r^2}[\frac{1}{c_1^2} K_2(i\frac{\omega r}{c_1}) - \frac{1}{c_2^2} K_2(i\frac{\omega r}{c_2})] + K_0(i\frac{\omega r}{c_2})/c_2^2 \\ &+ \frac{i}{\omega r c_1} K_1(i\frac{\omega r}{c_1}) - \frac{i}{\omega r c_2} K_1(i\frac{\omega r}{c_2})\}\end{aligned} \tag{3.27d}$$

$$\tilde{u}_{32}^*(0, y, z) = \tilde{u}_{23}^*(0, y, z) = \frac{1}{2\pi\rho}\frac{yz}{r^2}[\frac{1}{c_1^2} K_2(\frac{i\omega r}{c_1}) - \frac{1}{c_2^2} K_2(\frac{i\omega r}{c_2})] \tag{3.27e}$$

$$\begin{aligned}\tilde{u}_{33}^*(0, y, z) = \frac{1}{2\pi\rho}\{&\frac{z^2}{r^2}[\frac{1}{c_1^2} K_2(i\frac{\omega r}{c_1}) - \frac{1}{c_2^2} K_2(i\frac{\omega r}{c_2})] + K_0(i\frac{\omega r}{c_2})/c_2^2 \\ &+ \frac{i}{\omega r c_1} K_1(i\frac{\omega r}{c_1}) - \frac{i}{\omega r c_2} K_1(i\frac{\omega r}{c_2})\}\end{aligned} \tag{3.27f}$$

(2) When $\omega = 0$ (from equation (3.26a), $\beta = \frac{\Omega}{c} \neq 0$), the following limits can be derived:

$$\frac{K_0(p_1 r) - K_0(p_2 r)}{\omega^2} = \frac{r}{2\beta}(\frac{1}{c_1^2} - \frac{1}{c_2^2}) K_1(\beta r) \tag{3.28a}$$

$$\frac{K_1(p_1r)-K_1(p_2r)}{\omega^2}=\frac{r}{2\beta}\left(\frac{1}{c_1^2}-\frac{1}{c_2^2}\right)\left[K_0(\beta r)+\frac{1}{\beta r}K_1(\beta r)\right] \tag{3.28b}$$

$$\frac{K_2(p_1r)-K_2(p_2r)}{\omega^2}=\frac{r}{2\beta}\left(\frac{1}{c_1^2}-\frac{1}{c_2^2}\right)\left[K_1(\beta r)+\frac{2}{\beta r}K_2(\beta r)\right] \tag{3.28c}$$

Thus from equation (3.25),

$$\tilde{u}_{11}^*(\beta,y,z)=\frac{\beta r}{4\pi\rho}\left(\frac{1}{c_1^2}-\frac{1}{c_2^2}\right)K_1(\beta r) \tag{3.29a}$$

$$\tilde{u}_{21}^*(\beta,y,z)=\frac{i\beta y}{4\pi\rho}\left(\frac{1}{c_1^2}-\frac{1}{c_2^2}\right)\left[K_0(\beta r)+\frac{1}{\beta r}K_1(\beta r)\right] \tag{3.29b}$$

$$\tilde{u}_{31}^*(\beta,y,z)=\frac{i\beta z}{4\pi\rho}\left(\frac{1}{c_1^2}-\frac{1}{c_2^2}\right)\left[K_0(\beta r)+\frac{1}{\beta r}K_1(\beta r)\right] \tag{3.29c}$$

$$\begin{aligned}\tilde{u}_{22}^*(\beta,y,z)=\frac{1}{4\pi\rho}\Bigg\{&\frac{\beta y^2}{r}\left(\frac{1}{c_1^2}-\frac{1}{c_2^2}\right)\left[K_1(\beta r)+\frac{2}{\beta r}K_2(\beta r)\right]+2K_0(\beta r)/c_2^2\\&+\left(\frac{1}{c_1^2}-\frac{1}{c_2^2}\right)\left[K_0(\beta r)+\frac{1}{\beta r}K_1(\beta r)\right]\Bigg\}\end{aligned} \tag{3.29d}$$

$$\tilde{u}_{32}^*(\beta,y,z)=\frac{\beta}{4\pi\rho}\frac{yz}{r}\left(\frac{1}{c_1^2}-\frac{1}{c_2^2}\right)\left[K_1(\beta r)+\frac{2}{\beta r}K_2(\beta r)\right] \tag{3.29e}$$

$$\begin{aligned}\tilde{u}_{33}^*(\beta,y,z)=\frac{1}{4\pi\rho}\Bigg\{&\frac{\beta z^2}{r}\left(\frac{1}{c_1^2}-\frac{1}{c_2^2}\right)\left[K_1(\beta r)+\frac{2}{\beta r}K_2(\beta r)\right]+2K_0(\beta r)/c_2^2\\&+\left(\frac{1}{c_1^2}-\frac{1}{c_2^2}\right)\left[K_0(\beta r)+\frac{1}{\beta r}K_1(\beta r)\right]\Bigg\}\end{aligned} \tag{3.29f}$$

3.2.2.2 *Stationary harmonic load*

In this case, $\Omega\neq 0$ and $c=0$. There is only one situation that must be considered, i.e. when $\beta=0$. In this case equations (3.27) apply.

3.2.2.3 *Moving constant load*

In this case, $\Omega=0$ and $c\neq 0$. When $\beta=0$, ω also vanishes according to equation (3.26a). From equations (3.25), the displacement Green's functions in this case are given by

$$\tilde{u}_{11}^*=\frac{1}{2\pi\rho}\frac{1}{c_2^2} \tag{3.30a}$$

$$\tilde{u}^*_{21} = \tilde{u}^*_{12} = 0 \tag{3.30b}$$

$$\tilde{u}^*_{31} = \tilde{u}^*_{13} = 0 \tag{3.30c}$$

$$\tilde{u}^*_{22} \to -\frac{1}{2\pi\rho c_2^2} \ln\left(\sqrt{1 - c^2/c_2^2}\,\beta r\right) \tag{3.30d}$$

$$\tilde{u}^*_{32} = \tilde{u}^*_{23} = 0 \tag{3.30e}$$

$$\tilde{u}^*_{33} \to -\frac{1}{2\pi\rho c_2^2} \ln\left(\sqrt{1 - c^2/c_2^2}\,\beta r\right) \tag{3.30f}$$

Equations (3.30d) and (3.30f) show that the displacements $\tilde{u}^*_{22}$ and $\tilde{u}^*_{33}$ cannot be handled numerically in this case. However, since they are weakly singular at $\beta = 0$, there is no difficulty to convert the displacements from the wavenumber domain into the spatial domain by an inverse Fourier transform algorithm (e.g. FFT). This is demonstrated by the exact solution for an *undamped* homogeneous whole-space subject to a constant moving point load. This exact solution has been derived by Eason, Fulton and Sneddon [1955/1956]. The comparisons are shown in Figures 3.1 and 3.2 for the 'subsonic' case in which the load speed, 605 m/s, is slightly lower than the shear wave speed in the whole-space, 610 m/s (see Table 3.1). To produce the responses from the Fourier transformed moving Green's functions, the FFT technique is applied using 2048 samples with a spacing of β equal to $0.0025\times 2\pi$ rad/m. A high computational accuracy is achieved by the FFT, as shown in these two figures.

TABLE 3.1
Parameters for a whole-space

Young's modulus ($\times 10^6$ Nm^{-2})	Possion's ratio	Density (kg/m^3)	Loss factor	P-wave speed (m/s)	S-wave speed (m/s)
1770	0.4	1700	0.15	1500	610

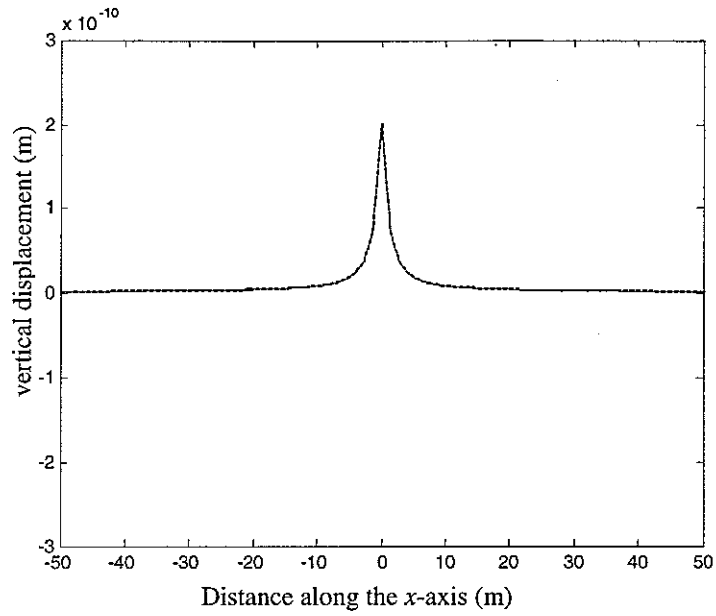

Figure 3.1. Vertical displacements along the straight line ($y = 0$ m, $z = 5$ m) due to a unit vertical constant load moving along the x-axis at 605 m/s. ——, from the Green's function via an inverse FFT; – – –, from the exact solution for a point moving load.

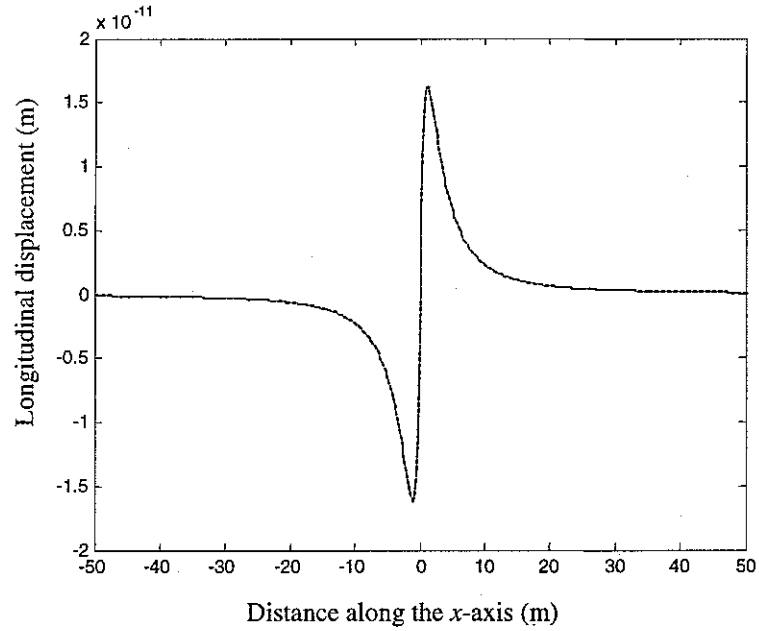

Figure 3.2. Longitudinal displacements along the straight line ($y = 0$ m, $z = 5$ m) due to a unit vertical constant load moving along the x-axis at 605 m/s. ——, from the Green's function; – – –, from the exact solution for a point moving load.

3.2.2.4 *Stationary constant load*

In this case, $\Omega = 0$ and $c = 0$, and therefore ω is always zero. This corresponds to an elastostatic problem, which is not the concern of this study.

3.2.3 *SINGULARITIES OF THE DISPLACEMENT GREEN'S FUNCTIONS*

The displacement Green's functions are singular at $r = 0$. The order of the singularities is summarized in Table 3.2.

TABLE 3.2. Singularities of the displacement Green's functions at $r = 0$

	$\beta = 0, \omega = \Omega \neq 0$ (Equation (27))	$\beta = 0, \omega = \Omega = 0$ (Equation (29))	$\beta \neq 0, \omega \neq 0$ (Equation (25))	$\beta = \Omega / c \neq 0, \omega = 0$ (Equation (29))
$\tilde{u}^*_{11}$	$\sim \ln(\frac{i\omega r}{c_2})$	$\sim \ln \omega r$	$\sim \ln p_2 r$	$\sim O(1)$
$\tilde{u}^*_{22}$	$\sim \ln(\frac{i\omega r}{c_2})$	$\sim 1/(\beta r)^2$	$\sim \ln p_2 r$	$\sim 1/(\beta r)^2$
$\tilde{u}^*_{33}$	$\sim \ln(\frac{i\omega r}{c_2})$	$\sim 1/(\beta r)^2$	$\sim \ln p_2 r$	$\sim 1/(\beta r)^2$
$\tilde{u}^*_{21}$	0	0	0	$1/(\beta r)$
$\tilde{u}^*_{31}$	0	0	0	$1/(\beta r)$
$\tilde{u}^*_{32}$	0	0	0	$1/(\beta r)$

Table 3.2 shows that, except for a particular value of β, the displacement Green's functions are, as in the case of the plane-strain problem, weakly singular at $r = 0$. The solution of the boundary integral equation (3.23) should be avoided for this particular value of β.

3.2.4 *STRESS GREEN'S FUNCTIONS AND SURFACE TRACTIONS*

The Fourier transformed moving stress Green's functions can be obtained following Hooke's law which, after being Fourier transformed, reads

$$\tilde{\tau}^*_{11l} = i\beta(\lambda + 2\mu)\tilde{u}^*_{1l} + \lambda(\frac{\partial \tilde{u}^*_{2l}}{\partial x_2} + \frac{\partial \tilde{u}^*_{3l}}{\partial x_3}) \tag{3.31a}$$

$$\tau^*_{22l} = i\beta\lambda\tilde{u}^*_{1l} + (\lambda + 2\mu)\frac{\partial \tilde{u}^*_{2l}}{\partial x_2} + \lambda\frac{\partial \tilde{u}^*_{3l}}{\partial x_3} \tag{3.31b}$$

$$\tau^*_{33l} = i\beta\lambda\tilde{u}^*_{1l} + \lambda\frac{\partial \tilde{u}^*_{2l}}{\partial x_2} + (\lambda + 2\mu)\frac{\partial \tilde{u}^*_{3l}}{\partial x_3} \tag{3.31c}$$

$$\tilde{\tau}^*_{23l} = \mu\left(\frac{\partial \tilde{u}^*_{3l}}{\partial x_2} + \frac{\partial \tilde{u}^*_{2l}}{\partial x_3}\right) \tag{3.31d}$$

$$\tilde{\tau}^*_{31l} = \mu\frac{\partial \tilde{u}^*_{1l}}{\partial x_3} + i\beta\mu\tilde{u}^*_{3l} \tag{3.31e}$$

$$\tilde{\tau}^*_{12l} = \mu\frac{\partial \tilde{u}^*_{1l}}{\partial x_2} + i\beta\mu\tilde{u}^*_{2l} \tag{3.31f}$$

where λ and μ are the Lamé constants.

The surface tractions are given by

$$\begin{Bmatrix} \tilde{p}^*_{1l} \\ \tilde{p}^*_{2l} \\ \tilde{p}^*_{3l} \end{Bmatrix} = \begin{bmatrix} \tilde{\tau}^*_{12l} & \tilde{\tau}^*_{13l} \\ \tilde{\tau}^*_{22l} & \tilde{\tau}^*_{23l} \\ \tilde{\tau}^*_{32l} & \tilde{\tau}^*_{33l} \end{bmatrix} \begin{Bmatrix} n_2 \\ n_3 \end{Bmatrix} \tag{3.32}$$

where, $\mathbf{n} = (0, n_2, n_3)$ is the unit normal vector at the surface, pointing outwards from the elastic body.

3.3 DISCRETIZATION USING QUADRATIC SHAPE FUNCTIONS

Following the general development of the BEM, the boundary integral equation is established by taking point (y_0, z_0) onto the boundary Γ in equation (3.23). This leads to

$$\begin{aligned} &\{\tilde{u}(\beta, y_0, z_0)\} \\ &= \int_\Gamma \left([\tilde{U}^*(-\beta, y, z; y_0, z_0)]^T \{\tilde{p}(\beta, y, z)\} - [\tilde{P}^*(-\beta, y, z; y_0, z_0)]^T \{\tilde{u}(\beta, y, z)\} \right) d\Gamma \\ &+ \int_A [\tilde{U}^*(-\beta, y, z; y_0, z_0)]^T \{\rho\tilde{b}(\beta, y, z)\} dA \end{aligned} \tag{3.33}$$

where, $(y_0, z_0) \in \Gamma$. A discretization is done for equation (3.33) and only a single type of boundary element is used. This type of element has three nodes and uses quadratic shape functions, as illustrated in Figure 3.3.

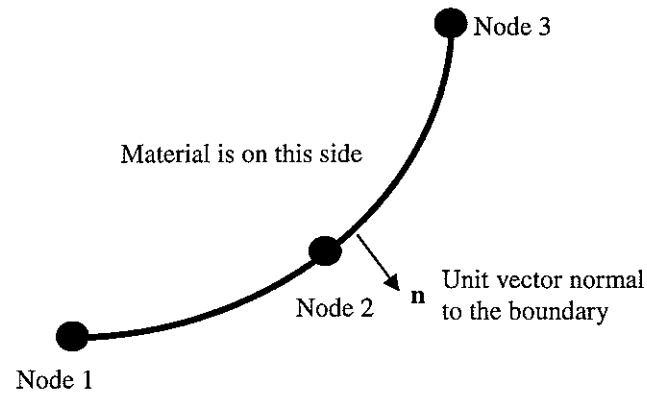

Figure 3.3. Three-noded, quadratic shape function boundary element

Let

$$\{\tilde{\mathbf{u}}(\beta)\}^j = (\tilde{u}_1^1, \tilde{u}_2^1, \tilde{u}_3^1, \tilde{u}_1^2, \tilde{u}_2^2, \tilde{u}_3^2, \tilde{u}_1^3, \tilde{u}_2^3, \tilde{u}_3^3)^T \tag{3.34}$$

$$\{\tilde{\mathbf{p}}(\beta)\}^j = (\tilde{p}_1^1, \tilde{p}_2^1, \tilde{p}_3^1, \tilde{p}_1^2, \tilde{p}_2^2, \tilde{p}_3^2, \tilde{p}_1^3, \tilde{p}_2^3, \tilde{p}_3^3)^T \tag{3.35}$$

be two 9×1 vectors consisting of the nodal displacements and tractions, respectively, for the 3 nodes in element *j*. Also let

$$\{\mathbf{y}\}^j = (y_1, z_1, y_2, z_2, y_3, z_3)^T \tag{3.36}$$

be a 6×1 vector consisting of the coordinates of the element nodes. Then the displacements, tractions and coordinates along the boundary element may be approximated by

$$\{\tilde{u}(\beta, y, z)\} = \{\tilde{u}(\beta, \xi)\} = [\Phi(\xi)]\{\tilde{\mathbf{u}}(\beta)\}^j \tag{3.37}$$

$$\{\tilde{p}(\beta, y, z)\} = \{\tilde{p}(\beta, \xi)\} = [\Phi(\xi)]\{\tilde{\mathbf{p}}(\beta)\}^j \tag{3.38}$$

$$(y, z)^T = [\Psi(\xi)]\{\mathbf{y}\}^j \tag{3.39}$$

where,

$$[\Phi(\xi)] = [\phi_1[I]_3 \;\; \phi_2[I]_3 \;\; \phi_3[I]_3], \; [\Psi(\xi)] = [\phi_1[I]_2 \;\; \phi_2[I]_2 \;\; \phi_3[I]_2] \tag{3.40}$$

are shape function matrices, $[I]_2$ and $[I]_3$ are the 2×2 and 3×3 unit matrices and

$$\phi_1(\xi)=\frac{1}{2}\xi(\xi-1),\phi_2(\xi)=(1-\xi^2),\phi_3(\xi)=\frac{1}{2}\xi(\xi+1),\quad(-1\le\xi\le 1) \tag{3.41}$$

are the shape functions.

Inserting equations (3.37), (3.38) and (3.39) into equation (3.33), and letting the point (y_0, z_0) be node i, yields

$$\begin{aligned}&\{\tilde{u}(\beta)\}^i+\sum_{j=1}^{NE}\left(\int_j[\tilde{P}^*(-\beta,\xi)]_{ij}^T[\Phi(\xi)]d\Gamma\right)\{\tilde{\mathbf{u}}(\beta)\}^j\\&=\sum_{j=1}^{NE}\left(\int_j[\tilde{U}^*(-\beta,\xi)]_{ij}^T[\Phi(\xi)]d\Gamma\right)\{\tilde{\mathbf{p}}(\beta)\}^j+\{\tilde{B}(\beta)\}^i\end{aligned} \tag{3.42}$$

where, $\{\tilde{u}(\beta)\}^i$ is the displacement vector of node i, $[\tilde{U}^*(-\beta,\xi)]_{ij}$ and $[\tilde{P}^*(-\beta,\xi)]_{ij}$ are the displacement and traction Green's function matrices with the source at node i (called *the collocation point*) and the observer located by equation (3.39) at boundary element Γ_j, NE is the number of elements and

$$\{\tilde{B}(\beta)\}^i=\int_A[\tilde{U}^*(-\beta,y,z;y_0,z_0)]^T\{\rho\tilde{b}(\beta,y,z)\}dA \tag{3.43}$$

represents the contribution from the body forces.

For a system of elements with a total of N nodes, equation (3.42) has the form

$$\{\tilde{u}(\beta)\}^i+\left[[\hat{H}]^{i1}\quad[\hat{H}]^{i2}\quad\cdots\quad[\hat{H}]^{iN}\right]\begin{Bmatrix}\tilde{u}_1^1\\\tilde{u}_2^1\\\tilde{u}_3^1\\\vdots\\\tilde{u}_1^N\\\tilde{u}_2^N\\\tilde{u}_3^N\end{Bmatrix}=\left[[G]^{i1}\quad[G]^{i2}\quad\cdots\quad[G]^{iN}\right]\begin{Bmatrix}\tilde{p}_1^1\\\tilde{p}_2^1\\\tilde{p}_3^1\\\vdots\\\tilde{p}_1^N\\\tilde{p}_2^N\\\tilde{p}_3^N\end{Bmatrix}+\{\tilde{B}(\beta)\}^i \tag{3.44}$$

where, $i = 1, 2, \ldots, N$. Here the element matrices, $[\hat{H}]^{ij}$ and $[G]^{ij}$ (both of them are 3×3 matrices) are assembled as in the finite element solution process. To make it clearer,

suppose node 3 is common to elements Γ_1 and Γ_2 (the other nodes for element Γ_1 are 1 and 2 and those for element Γ_2 are 4 and 5, see Figure 3.4). Letting

$$\begin{aligned}
&\int_{\Gamma_1} [\tilde{P}^*(-\beta,\xi)]_{i1}^T [\Phi(\xi)] d\Gamma \\
&= \int_{\Gamma_1} \left[\phi_1(\xi)[\tilde{P}^*(-\beta,\xi)]_{i1}^T \quad \phi_2(\xi)[\tilde{P}^*(-\beta,\xi)]_{i1}^T \quad \phi_3(\xi)[\tilde{P}^*(-\beta,\xi)]_{i1}^T\right] d\Gamma \\
&= \left[[\hat{h}]_1^{i1} \quad [\hat{h}]_1^{i2} \quad [\hat{h}]_1^{i3}\right]
\end{aligned} \tag{3.45}$$

$$\begin{aligned}
&\int_{\Gamma_2} [\tilde{P}^*(-\beta,\xi)]_{i2}^T [\Phi(\xi)] d\Gamma \\
&= \int_{\Gamma_2} \left[\phi_1(\xi)[\tilde{P}^*(-\beta,\xi)]_{i2}^T \quad \phi_2(\xi)[\tilde{P}^*(-\beta,\xi)]_{i2}^T \quad \phi_3(\xi)[\tilde{P}^*(-\beta,\xi)]_{i2}^T\right] d\Gamma \\
&= \left[[\hat{h}]_2^{i3} \quad [\hat{h}]_2^{i4} \quad [\hat{h}]_2^{i5}\right]
\end{aligned} \tag{3.46}$$

then

$$[\hat{H}]^{i2} = [\hat{h}]_1^{i2} \tag{3.47a}$$

$$[\hat{H}]^{i3} = [\hat{h}]_1^{i3} + [\hat{h}]_2^{i3} \tag{3.47b}$$

$$[\hat{H}]^{i4} = [\hat{h}]_2^{i4} \tag{3.47c}$$

Equation (3.44) may be written in a more compact form

$$[H]\{\tilde{\mathbf{u}}(\beta)\} = [G]\{\tilde{\mathbf{p}}(\beta)\} + \{\tilde{\mathbf{B}}(\beta)\} \tag{3.48}$$

where, $[H]$ and $[G]$ are $3N \times 3N$ matrices. This is the so-called (global) boundary element equation.

3.4 EVALUATION OF SINGULAR INTERGAL TERMS

In constructing the global equation (3.48) the integrals in equation (3.42) are evaluated for the Green's functions on each element making up the total integration around the boundary. For a collocation point not belonging to an element, the integrals along this element can be carried out using a standard numerical integration method. In the present study a 10-point Gauss-Legendre quadrature rule is used. The high order of this quadrature reflects the high polynomial order of the integrands.

When a collocation point is on an element the integrands become singular for both the evaluation of $[H]$ and $[G]$. The singular terms for constructing matrix $[G]$ may

be integrated after a special treatment that takes into account the presence in the integrands of a weak singularity which is of logarithmic order, as identified in Sub-section 3.2.3 an shown in Figures 3.4, 3.6 and 3.8. A commonly used method is to perform a non-linear transformation with a vanishing derivative of the first order at the singular point, so that the singularity in the integrands can be eliminated [Johnston and Johnston 2002, Singh and Tanaka 2001]. The integrals containing a singular term may be written in general as

$$I = \int_{-1}^{1} f(\xi) \ln(p_2 r) d\xi \tag{3.49}$$

where, $f(\xi)$ is a regular function and $r = r(\xi)$ vanishes at $\xi = -1, 0$ or 1 depending on the collocation point being the first, the second or the third node of the element. Without loss of generality, the collocation point is set to be the first node, so that $r(-1) = 0$. By applying transformation

$$\xi = \xi(t) = -1 + \frac{(1+t)^k}{2^{k-1}} \tag{3.50}$$

where k is a positive integer and $\xi'(-1) = 0$, then equation (3.49) becomes

$$I = \int_{-1}^{1} f(\xi(t)) \ln(p_2 r(\xi(t)) \xi'(t) dt \tag{3.51}$$

It can be shown that

$$\lim_{t \to -1} \ln(p_2 r(\xi(t)) \xi'(t) = 0, \text{ for } k \geq 2 \tag{3.52}$$

i.e. the integrand in equation (3.51) has no singularity, and can be integrated without any difficulty.

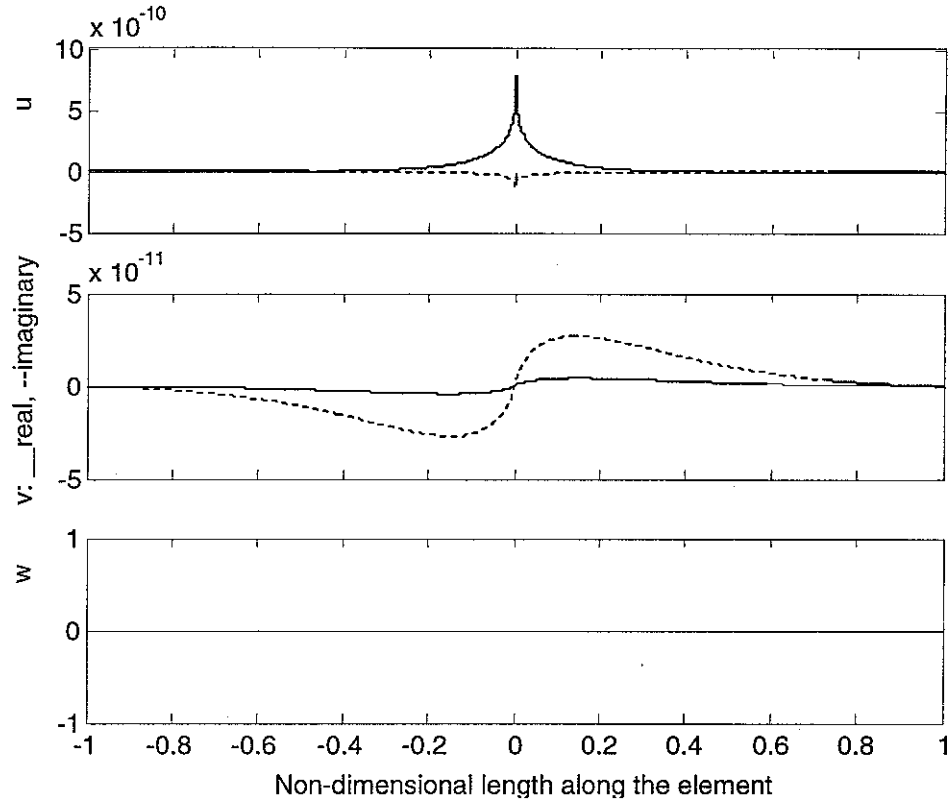

Figure 3.4. Displacements along a straight element due a longitudinal load applied at the middle node.

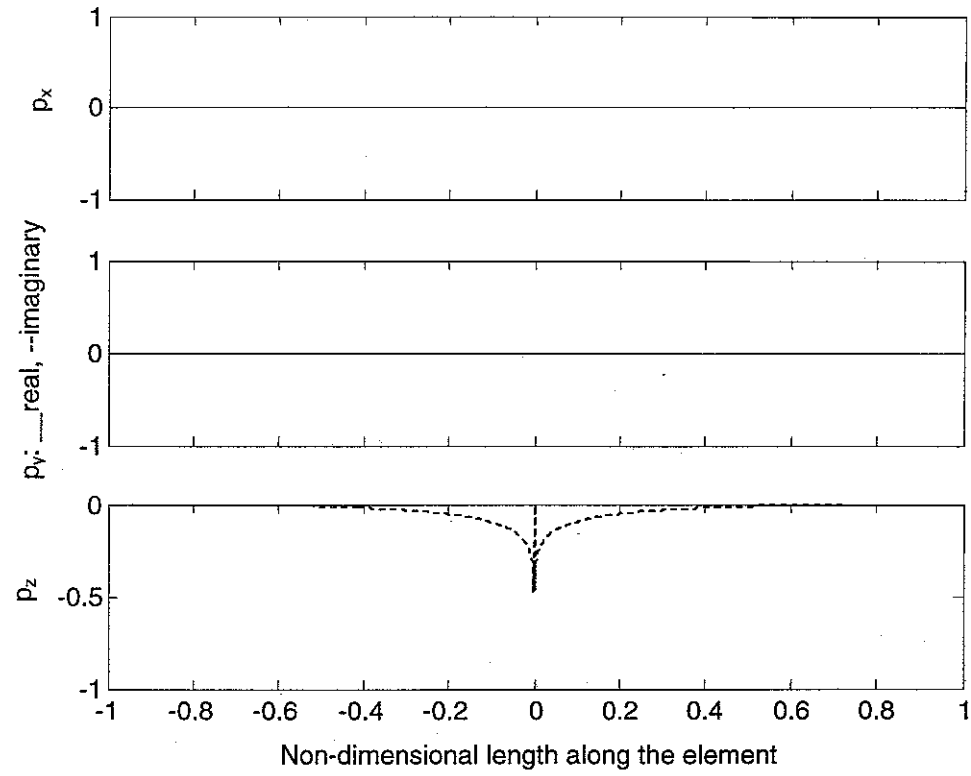

Figure 3.5. Tractions along a straight element due to a longitudinal load applied at the middle node.

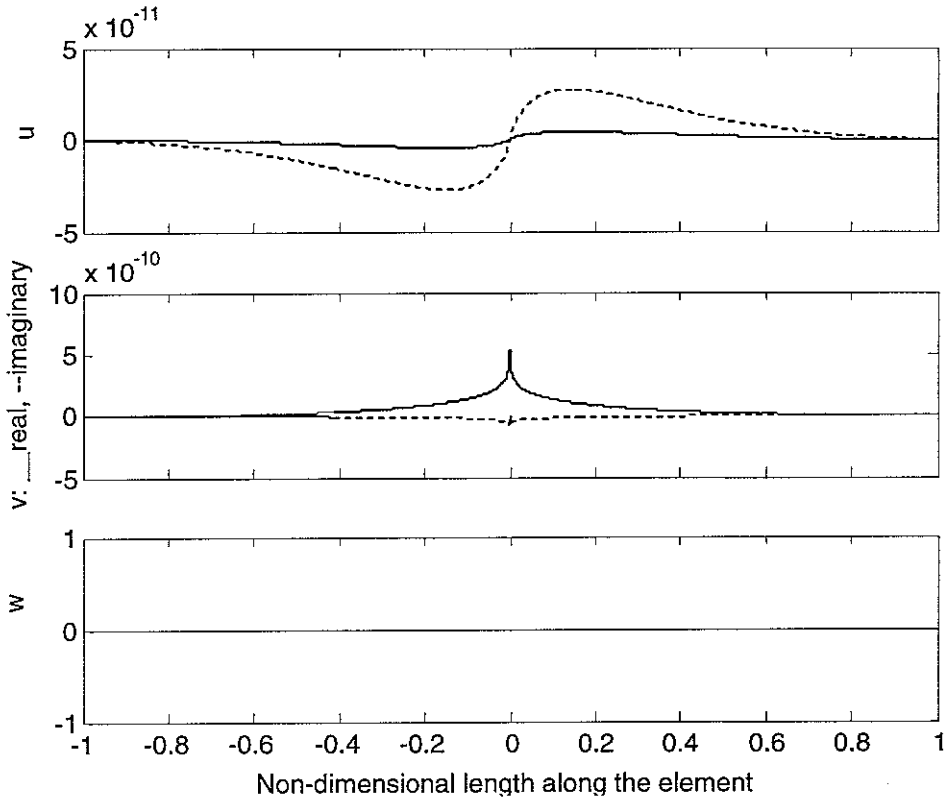

Figure 3.6. Displacements along a straight element due to a lateral load applied at the middle node.

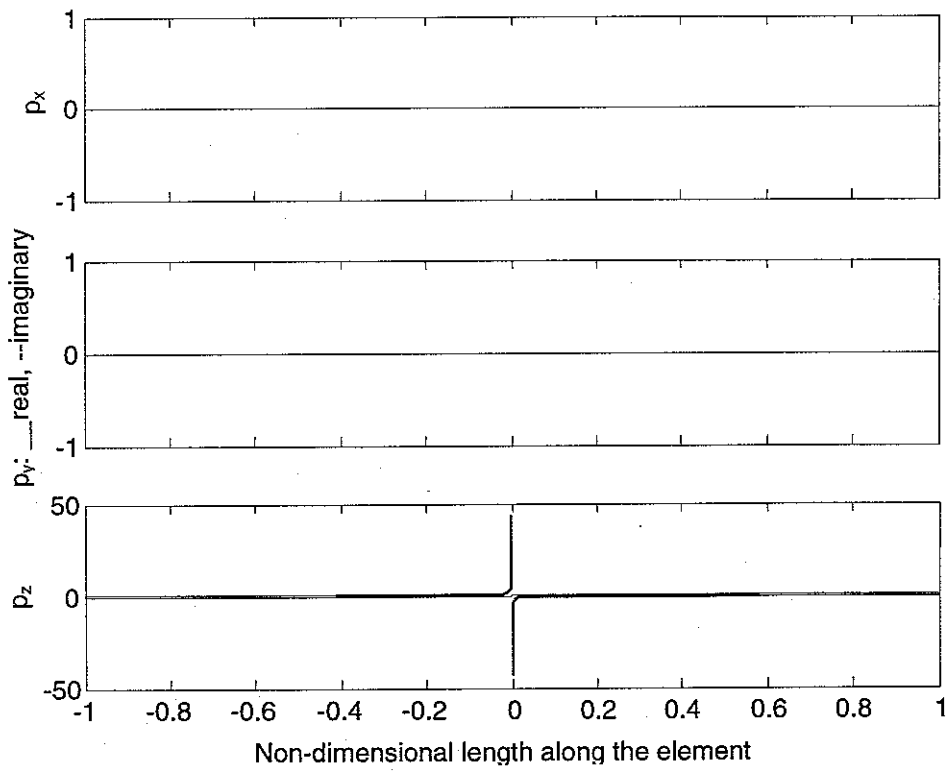

Figure 3.7. Tractions along an straight element due to a lateral load applied at the middle node.

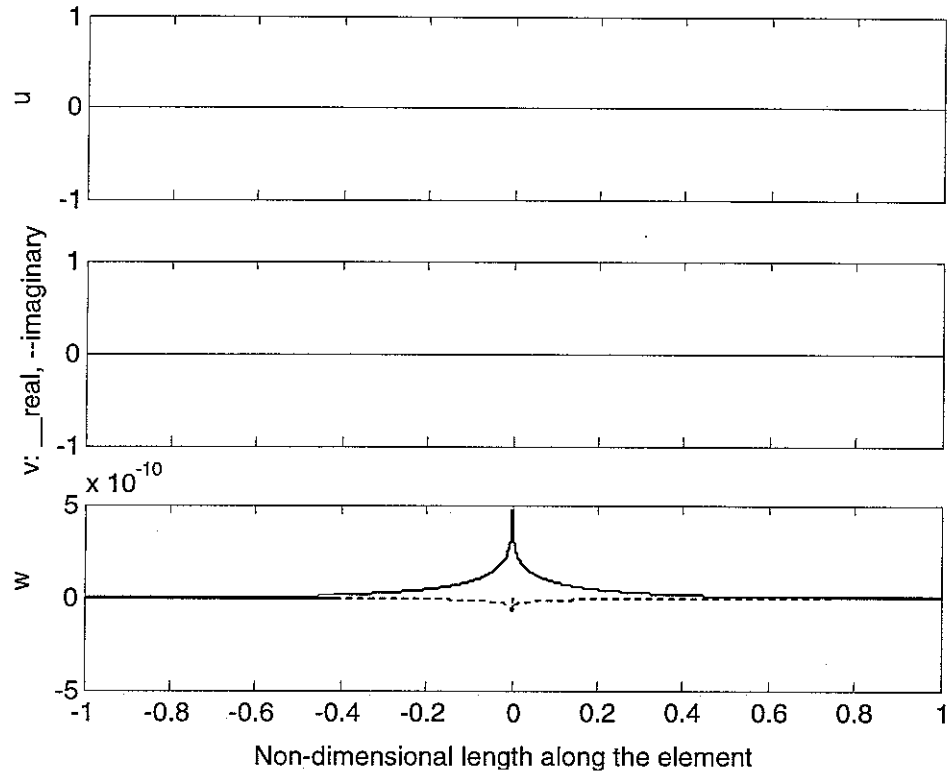

Figure 3.8. Displacements along a straight element due to a vertical load applied at the middle node.

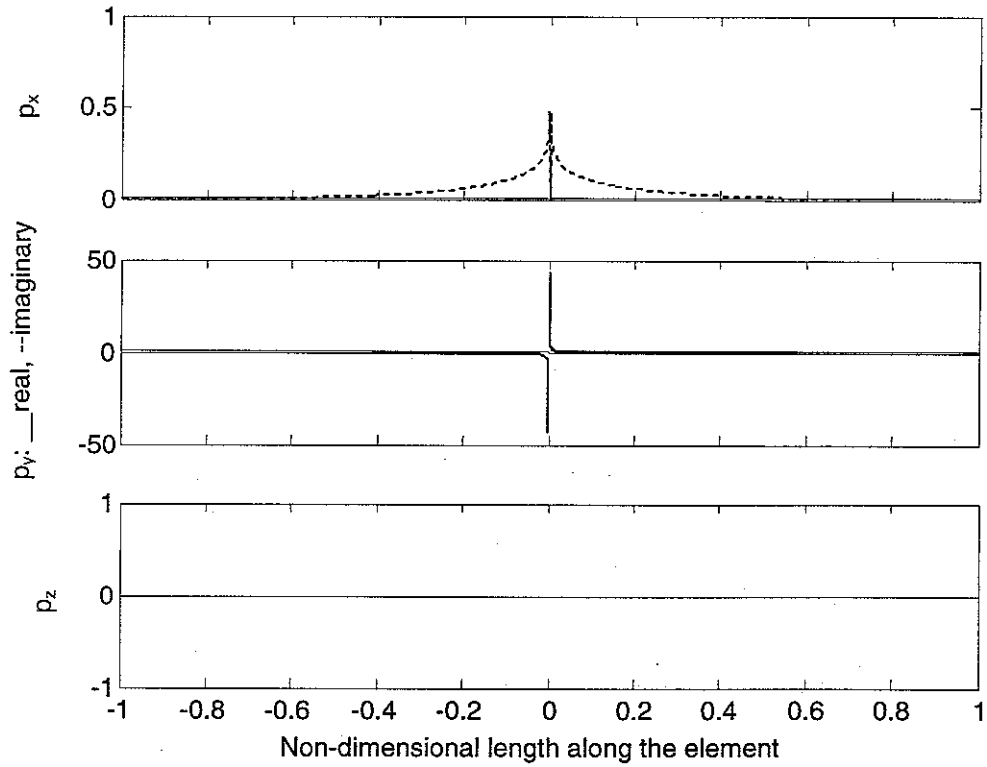

Figure 3.9. Tractions along a straight element due to a vertical load applied at the middle node.

The singular terms for constructing matrix $[H]$, however, are of higher order and are not integrable. This is shown in Figures 3.5, 3.7 and 3.9, where, tractions along a straight element due to a load applied at the middle node are plotted. The vanishing tractions in some subplots are true only at points which are not located at the middle node. At the middle node, the tractions can only be described by the δ-function in these subplots. However the integrations for these terms over a finite segment of the boundary containing the singular node have a finite result. This is because the integrands are either a δ-like function at the singular node or have singular terms of opposite signs either side of the node and these cancel. The implication of this is that the integral cannot be evaluated using any quadrature scheme on an element-by-element basis and an alternative method must be devised.

In the case of a stationary harmonic load, the difficulty may be overcome by employing the rigid body motion technique combined with either a fully or a locally enclosing elements technique [Jones, Thompson and Petyt 1999]. However, for the moving load case, this technique is inappropriate, since the strong singularity in the traction Green's functions corresponding to the static state is not easily identified. A new technique is therefore developed based on the FEM presented in Section 2.

As shown in Figure 3.10, boundary elements Γ_1 and Γ_2 have a common node 3. Suppose the two boundaries form an obtuse angle at node 3, then two finite elements may be formed by these two boundary elements plus 5 fictitious boundary elements (in dashed lines). Using eight-noded, quadratic shape functions and the two-and-half dimensional finite element method developed in Section 2, a global finite element equation can be formed for these two finite elements:

$$[K]'\begin{Bmatrix}\{\tilde{u}\}^1\\ \{\tilde{u}\}^2\\ \vdots\\ \{\tilde{u}\}^{13}\end{Bmatrix}=\begin{Bmatrix}\{\tilde{F}\}^1\\ \{\tilde{F}\}^2\\ \vdots\\ \{\tilde{F}\}^{13}\end{Bmatrix} \tag{3.53}$$

where, $[K]'$ is the global dynamic stiffness matrix of these two finite elements, $\{\tilde{u}\}^j$ and $\{\tilde{F}\}^j$ are, respectively, the nodal displacement vector and nodal force vector of node j (j = 1, 2, ..., 13). Suppose that, except for the tractions on boundaries Γ_1 to Γ_6,

there is no other excitation, then the nodal force vector $\{\tilde{F}\}^{13} = 0$. Thus from equation (3.53) the following equation can be derived

$$[K]\begin{Bmatrix}\{\tilde{u}\}^1\\ \{\tilde{u}\}^2\\ \vdots\\ \{\tilde{u}\}^{12}\end{Bmatrix} = \begin{Bmatrix}\{\tilde{F}\}^1\\ \{\tilde{F}\}^2\\ \vdots\\ \{\tilde{F}\}^{12}\end{Bmatrix} \tag{3.54}$$

Note that the tractions at nodes 1 to 12 have been assumed to be continuous. In other words, tractions 'before' and 'after' each of the nodes are the same. Tractions and displacements of boundaries Γ_1 to Γ_6 are interpolated by the values at the nodes. For example

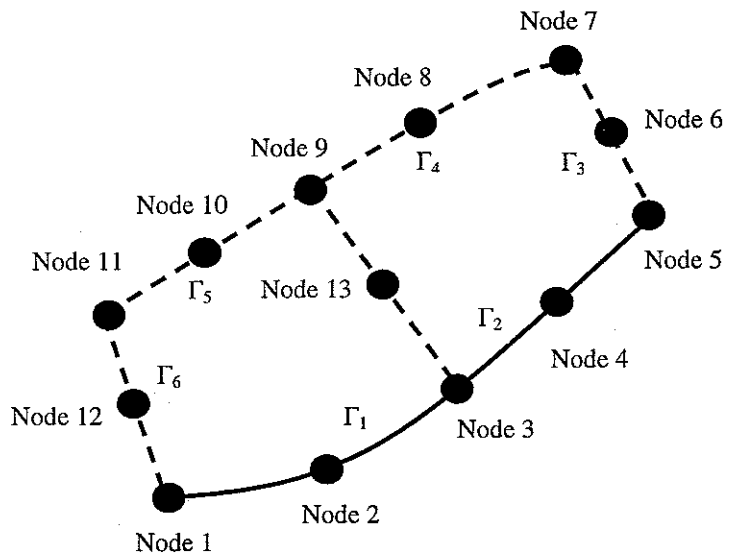

Figure 3.10. Two eight-noded, quadratic function finite elements.

$$\{\tilde{p}(\beta,y,z)\} = [\Phi(\xi)]\begin{Bmatrix}\{\tilde{p}\}^{11}\\ \{\tilde{p}\}^{12}\\ \{\tilde{p}\}^{1}\end{Bmatrix},\ \{\tilde{u}(\beta,y,z)\} = [\Phi(\xi)]\begin{Bmatrix}\{\tilde{u}\}^{11}\\ \{\tilde{u}\}^{12}\\ \{\tilde{u}\}^{1}\end{Bmatrix}\ (y,z)\in\Gamma_6 \tag{3.55a}$$

$$\{\tilde{p}(\beta,y,z)\} = [\Phi(\xi)]\begin{Bmatrix}\{\tilde{p}\}^{1}\\ \{\tilde{p}\}^{2}\\ \{\tilde{p}\}^{3}\end{Bmatrix},\ \{\tilde{u}(\beta,y,z)\} = [\Phi(\xi)]\begin{Bmatrix}\{\tilde{u}\}^{1}\\ \{\tilde{u}\}^{2}\\ \{\tilde{u}\}^{3}\end{Bmatrix}\ (y,z)\in\Gamma_1 \tag{3.55b}$$

$$\{\tilde{p}(\beta,y,z)\}=[\Phi(\xi)]\begin{Bmatrix}\{\tilde{p}\}^3\\ \{\tilde{p}\}^4\\ \{\tilde{p}\}^5\end{Bmatrix},\ \{\tilde{u}(\beta,y,z)\}=[\Phi(\xi)]\begin{Bmatrix}\{\tilde{u}\}^3\\ \{\tilde{u}\}^4\\ \{\tilde{u}\}^5\end{Bmatrix}\ (y,z)\in\Gamma_2 \tag{3.55c}$$

The virtual work done by the tractions is given by

$$\delta W=\sum_{j=1}^{6}\int_{\Gamma_j}\delta\{\tilde{u}\}^T\{\tilde{p}\}d\Gamma=\delta(\tilde{u}_1^1,\tilde{u}_2^1,\tilde{u}_3^1\cdots\tilde{u}_1^{12},\tilde{u}_2^{12},\tilde{u}_3^{12})[T]\begin{Bmatrix}\{\tilde{p}\}^1\\ \vdots\\ \{\tilde{p}\}^{12}\end{Bmatrix} \tag{3.56}$$

where $[T]$ is a symmetric, positive definite matrix of order 36×36, and is only dependent on the geometry of the boundary.

The same virtual work can be done by the equivalent nodal forces,

$$\delta W=\delta(\{\tilde{u}\}^{1T},\cdots\{\tilde{u}\}^{12T})\begin{Bmatrix}\{\tilde{F}\}^1\\ \{\tilde{F}\}^2\\ \vdots\\ \{\tilde{F}\}^{12}\end{Bmatrix} \tag{3.57}$$

Equations (3.56) and (3.57) give

$$\begin{Bmatrix}\{\tilde{F}\}^1\\ \vdots\\ \{\tilde{F}\}^{12}\end{Bmatrix}=[T]\begin{Bmatrix}\{\tilde{p}\}^1\\ \vdots\\ \{\tilde{p}\}^{12}\end{Bmatrix} \tag{3.58}$$

due to which, equation (3.54) becomes

$$[K]\begin{Bmatrix}\{\tilde{u}\}^1\\ \{\tilde{u}\}^2\\ \vdots\\ \{u\}^{12}\end{Bmatrix}=[T]\begin{Bmatrix}\{\tilde{p}\}^1\\ \{\tilde{p}\}^2\\ \vdots\\ \{\tilde{p}\}^{12}\end{Bmatrix} \tag{3.59}$$

For the domain shown in Figure 3.4, which is enclosed by six three-noded quadratic function boundary elements, a global boundary element equation can be written according to equation (3.48) (note: there is no body force)

$$[\hat{H}]\begin{Bmatrix}\{\tilde{u}\}^1\\ \{\tilde{u}\}^2\\ \vdots\\ \{\tilde{u}\}^{12}\end{Bmatrix}=[\hat{G}]\begin{Bmatrix}\{\tilde{p}\}^1\\ \{\tilde{p}\}^2\\ \vdots\\ \{\tilde{p}\}^{12}\end{Bmatrix}=[\hat{G}][T]^{-1}[K]\begin{Bmatrix}\{\tilde{u}\}^1\\ \{\tilde{u}\}^2\\ \vdots\\ \{\tilde{u}\}^{12}\end{Bmatrix} \tag{3.60}$$

which gives matrix $[\hat{H}]$ in terms of $[\hat{G}]$, $[T]$ and $[K]$, i.e.

$$[\hat{H}]=[\hat{G}][T]^{-1}[K] \tag{3.61}$$

The upper-left sub-matrix of $[\hat{H}]$ corresponding to nodes 1 to 5 is denoted by

$$\begin{bmatrix}[\hat{h}]_{11} & \cdots & [\hat{h}]_{15}\\ \vdots & \cdots & \vdots\\ [\hat{h}]_{51} & \cdots & [\hat{h}]_{55}\end{bmatrix} \tag{3.62}$$

where, for $i=1,2,\cdots 5$

$$[\hat{h}]_{i2}=\int_{\Gamma_1}\phi_2(\xi)[\tilde{P}^*(-\beta,\xi)]_{i1}^T d\Gamma \tag{3.63a}$$

$$[\hat{h}]_{i3}=\int_{\Gamma_1}\phi_3(\xi)[\tilde{P}^*(-\beta,\xi)]_{i1}^T d\Gamma+\int_{\Gamma_2}\phi_1(\xi)[\tilde{P}^*(-\beta,\xi)]_{i1}^T d\Gamma \tag{3.63b}$$

$$[\hat{h}]_{i4}=\int_{\Gamma_2}\phi_2(\xi)[\tilde{P}^*(-\beta,\xi)]_{i2}^T d\Gamma \tag{3.63c}$$

According to equation (3.48), the global boundary element equation of the original boundary element domain can be written as

$$[H]\{\tilde{\mathbf{u}}(\beta)\}=[G]\{\tilde{\mathbf{p}}(\beta)\}+\{\tilde{\mathbf{B}}(\beta)\} \tag{3.64}$$

The elements of $[H]$ associating with nodes 1 to 5 are given by

$$[H]^{i2}=\int_{\Gamma_1}\phi_2(\xi)[\tilde{P}^*(-\beta,\xi)]_{i1}^T d\Gamma \tag{3.65a}$$

$$[H]^{i3}=\int_{\Gamma_1}\phi_3(\xi)[\tilde{P}^*(-\beta,\xi)]_{i1}^T d\Gamma+\int_{\Gamma_2}\phi_1(\xi)[\tilde{P}^*(-\beta,\xi)]_{i1}^T d\Gamma \tag{3.65b}$$

$$[H]^{i4}=\int_{\Gamma_2}\phi_2(\xi)[\tilde{P}^*(-\beta,\xi)]_{i2}^T d\Gamma \tag{3.65c}$$

where, $i=1,2,\cdots 5$. It follows from equations (3.63) and (3.65) that

$$[H]^{ij} = [\hat{h}]_{ij},\ i = 1, 2, \cdots 5;\ j = 2, 3, 4 \tag{3.66}$$

Equation (3.66) gives the elements of matrix [H] not only for nodes belonging to the same element but also for those belonging to two adjacent elements.

It should be noted that equation (3.66) does not give accurate results in some cases. This may be overcome by adding extra nodes on the boundaries in Figure 3.10 and correspondingly constructing finer and therefore more finite elements. By this way both the FE equation (3.54) and the BE equation (3.60) are improved for the description of the motion of the 'structure' defined in Figure 3.10.

3.5 USE OF GEOMETRICAL SYMMETRY

Many problems involve structures that have at least one plane of geometrical symmetry. Examples include tunnels, tracks and many types of foundations. When the geometry is symmetric the load and the response may, in any case, be decomposed into symmetric and anti-symmetric parts. The symmetric part of the response is due to the symmetric part of the load while the anti-symmetric part of the response is due to the anti-symmetric part of the load. Use of the symmetry or anti-symmetry of the load-response configurations can reduce the size (by half or so) of matrices which are to be inverted in the boundary element method, therefore greatly improving the computational efficiency.

In what follows, the structure is assumed to be symmetric about the vertical plane $y = 0$ (so the cross-section of the structure is symmetric about the z-axis). The nodes in the half-plane $y \geq 0$ are numbered as 1, 2, ..., N. Of those N nodes, there are N_1 nodes, numbered as $j_1, j_2, \cdots j_{N_1}$, on the z-axis. Since three-noded elements are used, N_1 is definitely greater than zero though normally it is a small integer. The three degrees (in the x-, y- and z- directions) of freedom of node i ($i = 1, 2, \cdots N$) are numbered as $3(i-1)+1$, $3(i-1)+2$ and $3(i-1)+3$. The number of the mirror image node of node i, which is located in the half-plane $y < 0$, is denoted by i'. The three degrees of freedom of node i' are numbered as $3(i'-1)+1$, $3(i'-1)+2$ and $3(i'-1)+3$. The boundary element equation for this structure is given by equation (3.48), i.e.

$$[H]\{\tilde{\mathbf{u}}(\beta)\} = [G]\{\tilde{\mathbf{p}}(\beta)\} + \{\tilde{\mathbf{B}}(\beta)\} \tag{3.67}$$

where $[H]$ and $[G]$ are square matrices of order $3[2(N-N_1)+N_1]$.

When the loads on the structure are symmetric about $y = 0$, then it can be shown that, for nodes on the z-axis

$$\tilde{u}_{3(j-1)+2} = 0,\ \tilde{p}_{3(j-1)+2} = 0, \text{ where } j = j_1, j_2, \cdots j_{N_1} \tag{3.68a}$$

while for node i which is off the z-axis and its counterpart, node i',

$$\tilde{u}_{3(i'-1)+1} = \tilde{u}_{3(i-1)+1},\ \tilde{u}_{3(i'-1)+2} = -\tilde{u}_{3(i-1)+2},\ \tilde{u}_{3(i'-1)+3} = \tilde{u}_{3(i-1)+3} \tag{3.68b}$$

$$\tilde{p}_{3(i'-1)+1} = \tilde{p}_{3(i-1)+1},\ \tilde{p}_{3(i'-1)+2} = -\tilde{p}_{3(i-1)+2},\ \tilde{p}_{3(i'-1)+3} = \tilde{p}_{3(i-1)+3} \tag{3.68c}$$

Similarly, when the loads on the structure are anti-symmetric about $y = 0$, then for nodes on the z-axis

$$\tilde{u}_{3(j-1)+1} = \tilde{p}_{3(j-1)+1} = 0,\ \tilde{u}_{3(j-1)+3} = \tilde{p}_{3(j-1)+3} = 0 \tag{3.69a}$$

where $j = j_1, j_2, \cdots j_{N_1}$; for nodes i and i' which are off the z-axis

$$\tilde{u}_{3(i'-1)+1} = -\tilde{u}_{3(i-1)+1},\ \tilde{u}_{3(i'-1)+2} = \tilde{u}_{3(i-1)+2},\ \tilde{u}_{3(i'-1)+3} = -\tilde{u}_{3(i-1)+3} \tag{3.69b}$$

$$\tilde{p}_{3(i'-1)+1} = -\tilde{p}_{3(i-1)+1},\ \tilde{p}_{3(i'-1)+2} = \tilde{p}_{3(i-1)+2},\ \tilde{p}_{3(i'-1)+3} = -\tilde{p}_{3(i-1)+3} \tag{3.69c}$$

A size-reduced equation now can be produced by keeping the first $3N$ equations in (3.67) and then using equations (3.68b and c) or (3.69b and c) to eliminate the displacements and tractions of the image nodes. For future use, the equation for the symmetric load/response configuration is denoted by

$$[H]^+\{\tilde{\mathbf{u}}(\beta)\}^+ = [G]^+\{\tilde{\mathbf{p}}(\beta)\}^+ + \{\tilde{\mathbf{B}}(\beta)\}^+ \tag{3.70}$$

while that for the anti-symmetric load/response configuration is denoted by

$$[H]^-\{\tilde{\mathbf{u}}(\beta)\}^- = [G]^-\{\tilde{\mathbf{p}}(\beta)\}^- + \{\tilde{\mathbf{B}}(\beta)\}^- \tag{3.71}$$

To ensure that the matrices $[H]^+$, $[G]^+$, $[H]^-$ and $[G]^-$ are regular (invertible), the zero displacements and tractions at the on-z-nodes, e.g. equations (3.68a) and (3.69a), must not be applied when constructing equations (3.70) and (3.71). Instead, such

displacements and tractions are kept as unknowns in the construction of these two equations.

3.6 EQUAVALENT DYNAMIC STIFFNESS MATRIX

Equation (3.48) gives the global boundary element equation. If there is no body force applied within the boundary element domain, i.e. $\{\tilde{\mathbf{B}}(\beta)\} = 0$, then equation (3.48) yields

$$[G]^{-1}[H]\{\tilde{\mathbf{u}}(\beta)\} = \{\tilde{\mathbf{p}}(\beta)\} \tag{3.72}$$

which associates the nodal (on the boundary)displacements and the nodal tractions. Similar to equation (3.58), a transformation matrix can be constructed between the nodal tractions and the nodal forces for the boundary element domain such that

$$\{\tilde{\mathbf{F}}(\beta)\} = [T]\{\tilde{\mathbf{p}}(\beta)\} \tag{3.73}$$

which, combined with equation (3.72), gives

$$[T][G]^{-1}[H]\{\tilde{\mathbf{u}}(\beta)\} = \{\tilde{\mathbf{F}}(\beta)\} \tag{3.74}$$

A matrix $[K(\beta)]_{be}$ is defined by

$$[K(\beta)]_{be} = [T][G]^{-1}[H] \tag{3.75}$$

and is termed *the BE dynamic stiffness matrix* of the boundary element domain. It should be noted that this dynamic stiffness matrix does not have the usual FE property of symmetry, which is a disadvantage with respect to memory storage space. Mustoe [1980] suggested a method by which a symmetric boundary element stiffness matrix can be produced. However this method requires the inversion of a matrix twice the size of $[K(\beta)]_{be}$ and therefore is very time consuming. Tullberg and Bolteus [1982] conducted a study of seven different stiffness matrices for a BE domain, including the original non-symmetric stiffness matrix given in equation (3.75) and six symmetric matrices. They concluded that:

(1) The non-symmetric stiffness matrix given in equation (3.75) is the best in terms of accuracy.

(2) The non-symmetric stiffness matrix is as good as, or better than, a stiffness matrix based on a finite element discretization with the same number of degrees of freedom.

(3) The manipulated methods involving symmetric matrices show a very poor rate of convergence compared to the direct BE.

3.7 VALIDATION

The discrete wavenumber boundary element method developed in the section (Sub-sections 3.1 to 3.6) and the corresponding computer program have been validated by (1) calculating the response of a homogeneous whole-space including a circular unlined tunnel; (2) calculating the response of a homogeneous half-space; (3) calculating the response of a homogeneous half-space with an unlined tunnel.

3.7.1 *FOR A HOMOGENEOUS WHOLE-SPACE WITH A CIRCULAR UNLINED TUNNEL*

The discrete wavenumber boundary element method and the corresponding computer program can be validated by calculating the response of a homogeneous whole-space including a circular unlined tunnel subject to a moving harmonic load. The analytical solution (called *the 'cylinder theory'*) for such a structure subject to moving harmonic loads has been derived by the present authors [Sheng, Jones and Thompson 2002]. The parameters of material are listed in Table 3.1. The radius of the tunnel is 3.5 m and the tunnel axis is set to be the x-axis.

Figures 3.11 to 3.13 present comparisons between the BEM solution and the analytical solution. In the boundary element mesh, 30 three-noded quadrilateral elements are used along the tunnel surface. In the performance of the FFT, 2048 samples are used with a spacing of β equal to $0.0025\times 2\pi$ (rad/m).

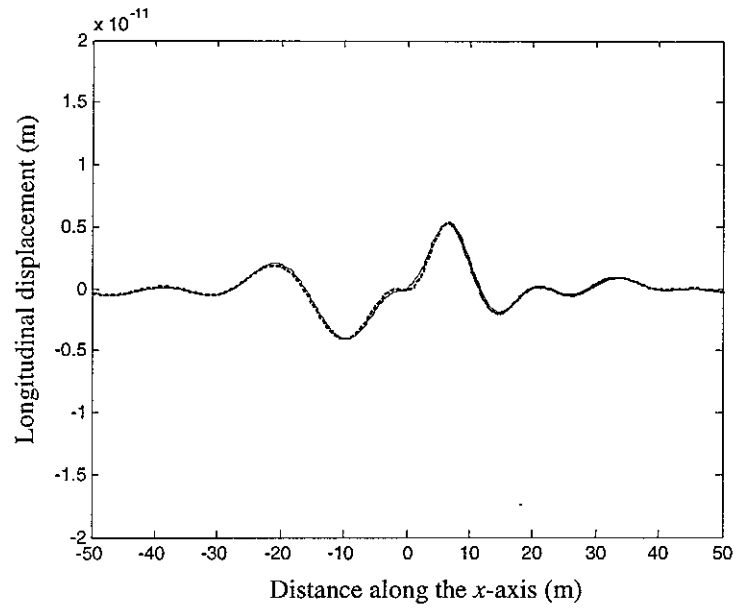

Figure 3.11. Longitudinal displacement along the straight line ($y = 0$ m, $z = -3.5$ m) due to a unit lateral harmonic load of 40 Hz moving at 100 m/s along the straight line ($y = 5$ m, $z = 0$ m). ——, calculated by the cylinder theory; – – –, calculated by BEM.

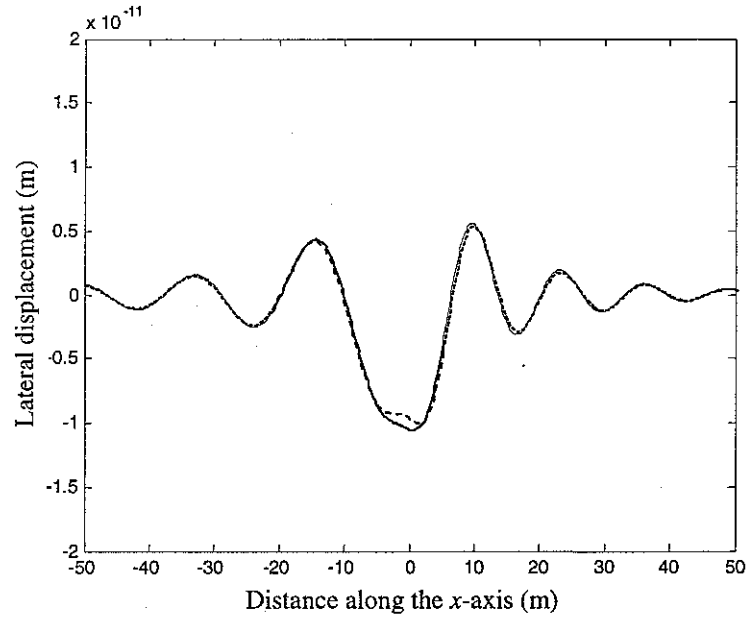

Figure 3.12. Lateral displacement along the straight line ($y = 0$ m, $z = -3.5$ m) due to a unit lateral harmonic load of 40 Hz moving at 100 m/s along the straight line ($y = 5$ m, $z = 0$ m). ——, calculated by the cylinder theory; – – –, calculated by BEM.

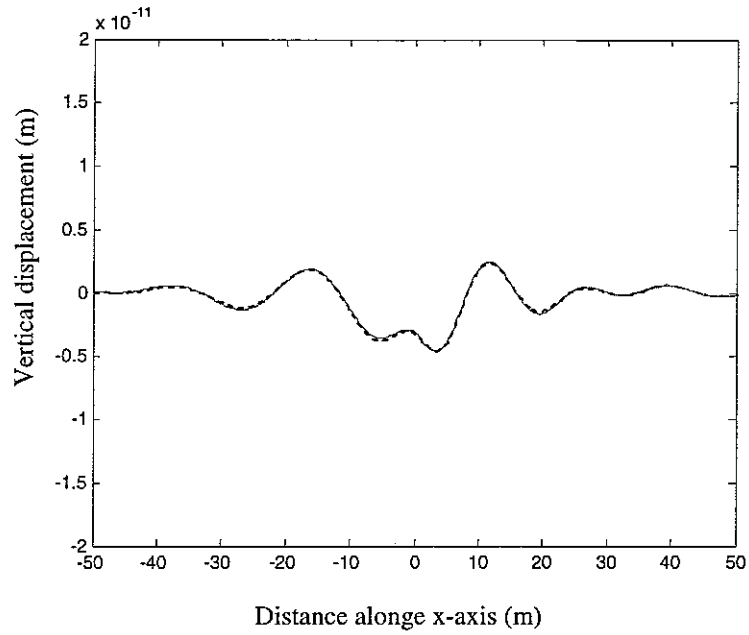

Figure 3.13.Vertical displacement along the straight line ($y = 0$ m, $z = -3.5$ m) due to a unit lateral harmonic load of 40 Hz moving at 100 m/s along the straight line ($y = 5$ m, $z = 0$ m). ——, calculated by the cylinder theory; – – –, calculated by BEM.

3.7.2 *FOR A HOMOGENEOUS HALF-SPACE*

The responses of a homogeneous half-space to surface or buried moving harmonic loads can be evaluated using the approach presented in [Sheng, Jones and Petyt 1999] (called *the layered ground model*). Comparisons between this approach and the BEM are shown in Figures 3.8 to 3.11. The load is a unit (1 N) vertical point harmonic load moving at 100 m/s in the x-direction. Figures 3.14 and 3.15 present the results for a load of 40 Hz acting at a depth of 3 m while Figures 3.16 and 3.17 account for a load of 200 Hz acting at a depth of 20 m. In the boundary element model a mesh of 50 elements (for one side on the ground surface over 50 m) has been employed. In other words, there are three elements per Rayleigh wavelength (about 3 m at 200 Hz at 100 m/s). In the performance of the inverse FFT, 1024 samples are used with a spacing of β equal to $0.0025 \times 2\pi$ (rad/m). As can be seen, a good accuracy has been achieved.

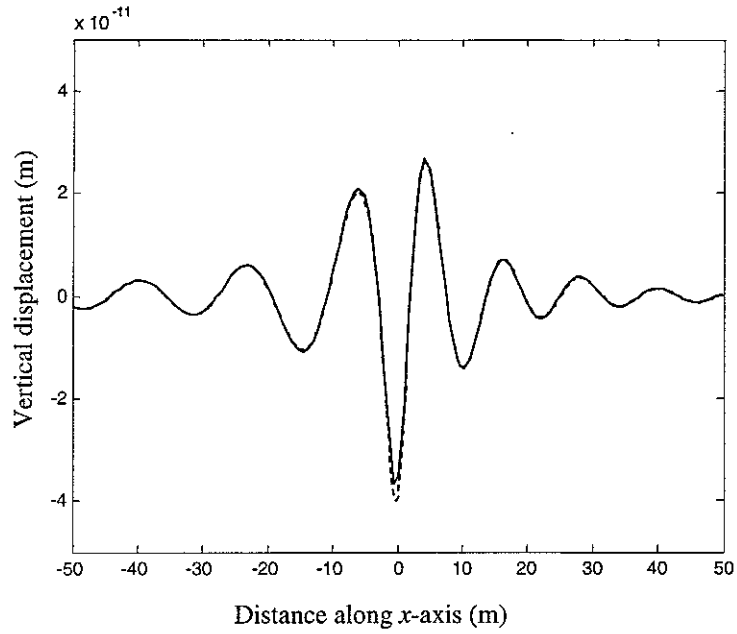

Figure 3.14.Vertical displacement along the x-axis on the ground surface due to a unit vertical harmonic load of 40 Hz moving at 100 m/s along the straight line (y = 0 m, z = -3 m) at a depth of 3 m. —, calculated by the layered ground model; – – –, calculated by BEM.

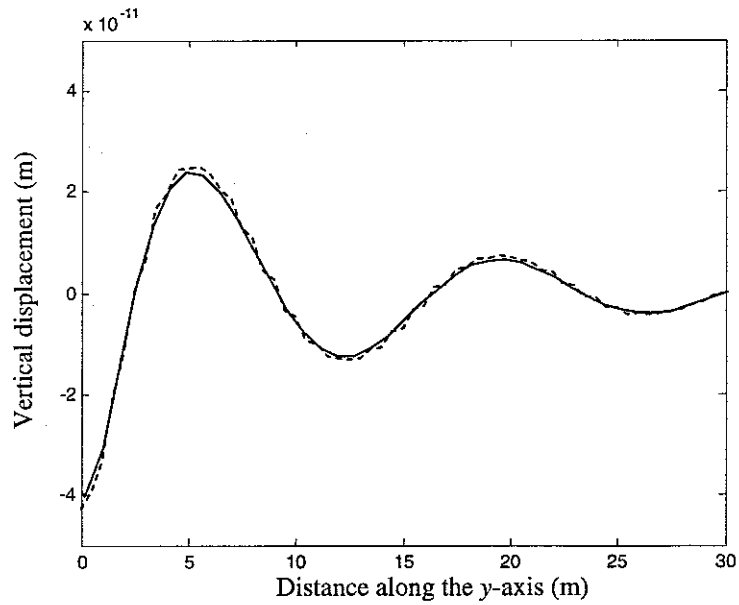

Figure 3.15.Vertical displacement along the y-axis on the ground surface due to a unit vertical harmonic load of 40 Hz moving at 100 m/s along the straight line (y = 0 m, z = -3 m) at a depth of 3 m. —, calculated by the layered ground model; – – –, calculated by BEM.

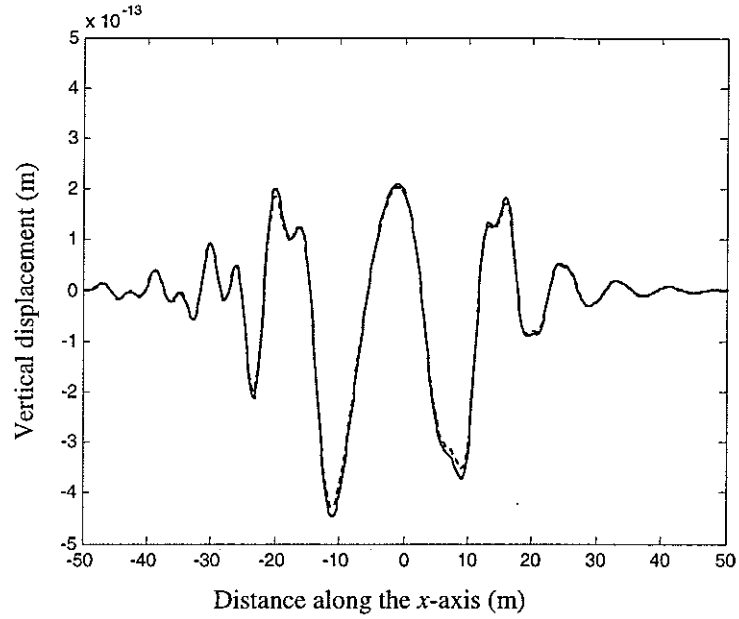

Figure 3.16.Vertical displacement along the x-axis on the ground surface due to a unit vertical harmonic load of 200 Hz moving at 100 m/s along the straight line (y = 0 m, z = -20 m) at a depth of 20 m. ——, calculated by the layered ground model; – – –, calculated by BEM.

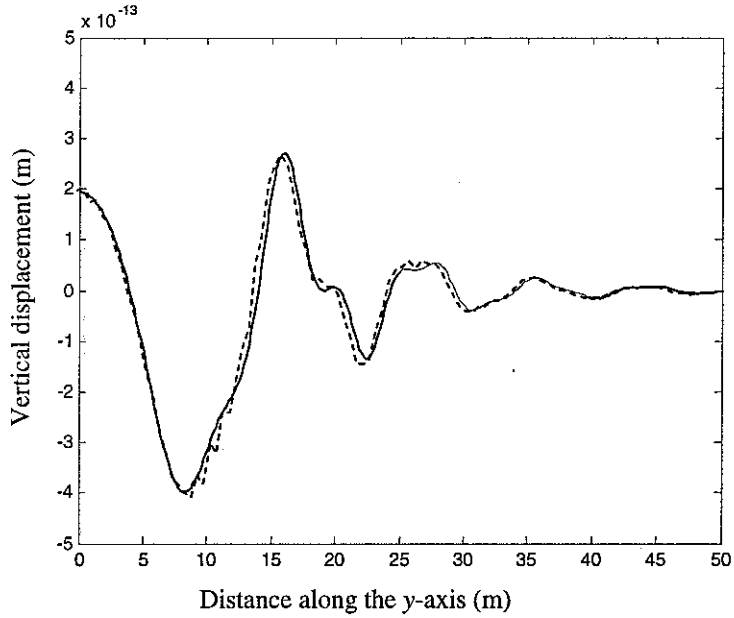

Figure 3.17.Vertical displacement along the y-axis on the ground surface due to a unit vertical harmonic load of 200 Hz moving at 100 m/s along the straight line (y = 0 m, z = -20 m) at a depth of 20 m. ——, calculated by the layered ground model; – – –, calculated by BEM.

3.7.3 *FOR A HOMOGENEOUS HALF-SPACE WITH AN UNLINED TUNNEL*

Responses of a layered ground with a circular tunnel to moving harmonic loads have been recently modelled using *the discrete wavenumber fictitious force method*

[Sheng, Jones and Thompson 2002]. This modelling approach is based on the Green's functions for a layered ground and those for a circular cylinder. Comparison between this approach and the boundary element approach are in Figures 3.18 and 3.19. The tunnel has a radius of 3.5 m and its axis is at 16.5 below the ground surface. In the boundary element model, 80 elements (one side) have been used with an element length equal to 0.625 m for the ground surface and 20 elements (one side, the length of each element is 0.55 m) for the tunnel surface. In the performance of the inverse FFT, 1024 samples are used with a spacing of β equal to $0.0025\times 2\pi$ (rad/m). It can be seen high consistency has been achieved between these two methods.

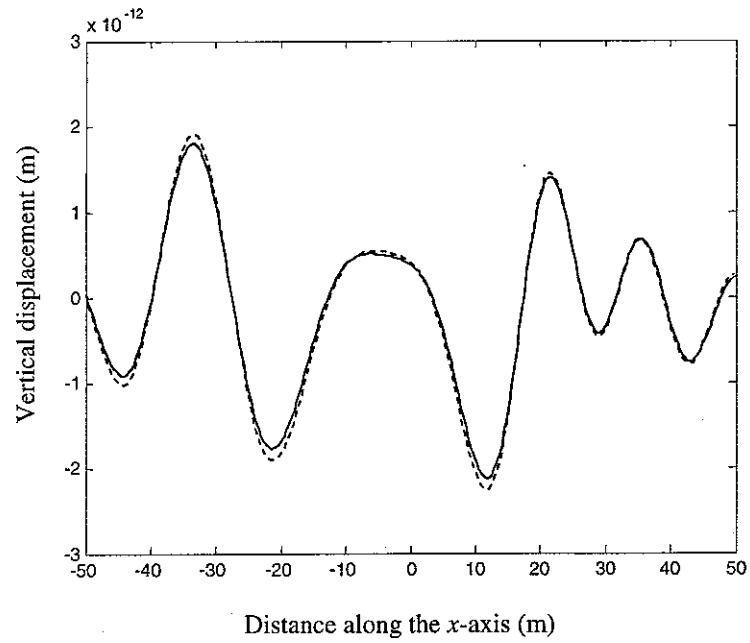

Figure 3.18.Vertical displacement along the x-axis on the ground surface due to a unit vertical harmonic load of 40 Hz at the tunnel invert and moving at 100 m/s in the tunnel direction. ——, calculated by the discrete wavennumber fictitious force method; – – –, calculated by BEM.

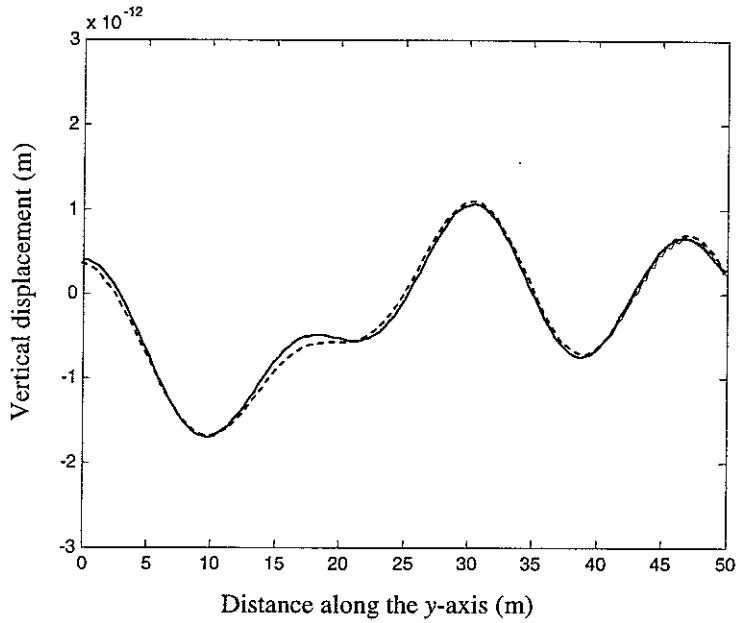

Figure 3.19.Vertical displacement along the y-axis on the ground surface due to a unit vertical harmonic load of 40 Hz at the tunnel invert and moving at 100 m/s in the tunnel direction. ——, calculated by the discrete wavennumber fictitious force method; – – –, calculated by BEM.

4. COUPLING BETWEEN FINITE/BOUNDARY ELEMENT DOMIANS

Up to now formulation has been derived in Section 3 for a boundary element model of a domain consisting of a single homogeneous material. A domain such as a layered ground with an arbitrary geometry of the ground surface and interfaces, which may also incorporates built structures, can be divided into a number of sub-domains each of which is homogeneous. For each sub-domain, a boundary element equation or a finite element equation can be constructed using the formulations derived in Sections 2 and 3. In this study, it is assumed that, at most, only one finite element sub-domain is present, and the finite element equation is given by

$$[K]_{fe}\{\tilde{u}(\beta)\} = \{\tilde{F}(\beta)\} \tag{4.1}$$

where, $[K]_{fe}$ denotes the dynamic stiffness matrix of the finite element sub-domain, $\{\tilde{u}(\beta)\}$ denotes the nodal displacement vector and $\{\tilde{F}(\beta)\}$ denotes the nodal force vector. For each boundary element sub-domain, the boundary element equation is given by

$$[H]_{ibe}\{\tilde{u}(\beta)\} = [G]_{ibe}\{\tilde{p}(\beta)\} + \{\tilde{B}(\beta)\}_{ibe} \tag{4.2}$$

where the subscript *ibe* is used to denote a boundary element sub-domain number. Equation (4.2) yields

$$[R]_{ibe}\{\tilde{u}(\beta)\} = \{\tilde{p}(\beta)\} + \{\tilde{s}(\beta)\}_{ibe} \tag{4.3}$$

where,

$$[R]_{ibe} = [G]_{ibe}^{-1}[H]_{ibe} \tag{4.4}$$

$$\{\tilde{s}(\beta)\}_{ibe} = [G]_{ibe}^{-1}\{\tilde{B}(\beta)\}_{ibe} \tag{4.5}$$

The coupling between the boundary element sub-domains and the finite element sub-domain is established on the basis of continuity of the displacement and equilibrium of the forces at the interfaces. The equilibrium of the forces at the interfaces can be expressed in terms of either tractions or nodal forces. In this study the coupling between two boundary element sub-domains is performed in terms of the equilibrium of the tractions on the interface while that between a boundary element sub-domain and a finite element sub-domain is achieved by the use of the equilibrium of the nodal forces on the interface.

4.1 COUPLING OF TWO BOUNDARY ELEMENT SUB-DOMAINS

Suppose boundary element sub-domain 1 has an interface with boundary element sub-domain 2. The displacement and traction vectors of the nodes on the interface are denoted by $\{\tilde{u}(\beta)\}_I$ and $\{\tilde{p}(\beta)\}_I$, and those of the remaining nodes are denoted by $\{\tilde{u}(\beta)\}_{1R}, \{\tilde{p}(\beta)\}_{1R}$ for sub-domain 1 and $\{\tilde{u}(\beta)\}_{2R}, \{\tilde{p}(\beta)\}_{2R}$ for sub-domain 2. It follows from equation (4.3) that

$$\begin{bmatrix}[R]_{1RR} & [R]_{1RI}\\ [R]_{1IR} & [R]_{1II}\end{bmatrix}\begin{Bmatrix}\{\tilde{u}(\beta)\}_{1R}\\ \{\tilde{u}(\beta)\}_I\end{Bmatrix} = \begin{Bmatrix}\{\tilde{p}(\beta)\}_{1R}\\ \{\tilde{p}(\beta)\}_I\end{Bmatrix} + \begin{Bmatrix}\{\tilde{s}(\beta)\}_{1R}\\ \{\tilde{s}(\beta)\}_{1I}\end{Bmatrix} \tag{4.6}$$

$$\begin{bmatrix}[R]_{2II} & [R]_{2IR}\\ [R]_{2RI} & [R]_{2RR}\end{bmatrix}\begin{Bmatrix}\{\tilde{u}(\beta)\}_I\\ \{\tilde{u}(\beta)\}_{2R}\end{Bmatrix} = \begin{Bmatrix}-\{\tilde{p}(\beta)\}_I\\ \{\tilde{p}(\beta)\}_{2R}\end{Bmatrix} + \begin{Bmatrix}\{\tilde{s}(\beta)\}_{2I}\\ \{\tilde{s}(\beta)\}_{2R}\end{Bmatrix} \tag{4.7}$$

Now $\{\tilde{p}(\beta)\}_I$ can be eliminated from equations (4.6) and (4.7), and an equation governing the remaining unknowns is therefore produced,

$$\begin{bmatrix} [R]_{1RR} & [R]_{1RI} & 0 \\ [R]_{1IR} & [R]_{1II}+[R]_{2II} & [R]_{2IR} \\ 0 & [R]_{2RI} & [R]_{2RR} \end{bmatrix} \begin{Bmatrix} \{\tilde{u}(\beta)\}_{1R} \\ \{\tilde{u}(\beta)\}_{I} \\ \{\tilde{u}(\beta)\}_{2R} \end{Bmatrix} = \begin{Bmatrix} \{\tilde{p}(\beta)\}_{1R} \\ 0 \\ \{\tilde{p}(\beta)\}_{2R} \end{Bmatrix} + \begin{Bmatrix} \{\tilde{s}(\beta)\}_{1R} \\ \{\tilde{s}(\beta)\}_{1I}+\{\tilde{s}(\beta)\}_{2I} \\ \{\tilde{s}(\beta)\}_{2R} \end{Bmatrix} \quad (4.8)$$

Equation (4.8) shows that the 'global equation' of the two sub-domains can be assembled in the finite element sense.

4.2 COUPLING OF A BOUNDARY ELEMENT DOMAIN AND A FINITE ELEMENT DOMAIN

Using the method presented in Section 4.1, a boundary element equation may be constructed for all the boundary element sub-domains. This equation relates the displacements at all the boundaries and interfaces to the boundary tractions as well as the externally exerted loads. This equation may be written, according to equation (4.8), as

$$[R]_{be}\{\tilde{u}(\beta)\} = \{\tilde{p}(\beta)\} + \{\tilde{s}(\beta)\}_{be} \quad (4.9)$$

Note that, elements in vector $\{\tilde{p}(\beta)\}$ vanish if they correspond to the nodes at the interfaces. If, in addition to the boundary element sub-domains, a finite element sub-domain is present, then the finite element equation (4.1) must be coupled with equation (4.9) to give the global equation for the whole model. The displacements, tractions and nodal forces of the nodes at the finite/boundary element domain interface are denoted by $\{\tilde{u}(\beta)\}_I$, $\{\tilde{p}(\beta)\}_I$ and $\{\tilde{F}(\beta)\}_I$. Those of the remaining nodes are denoted by $\{\tilde{u}(\beta)\}_{beR}$ and $\{\tilde{p}(\beta)\}_{beR}$ for the boundary sub-domains, and $\{\tilde{u}(\beta)\}_{feR}$, $\{\tilde{F}(\beta)\}_{feR}$ for the finite element sub-domain. Thus equation (4.9) can be split into

$$\begin{bmatrix} [R]_{beRR} & [R]_{beRI} \\ [R]_{beIR} & [R]_{beII} \end{bmatrix} \begin{Bmatrix} \{\tilde{u}(\beta)\}_{beR} \\ \{\tilde{u}(\beta)\}_{I} \end{Bmatrix} = \begin{Bmatrix} \{\tilde{p}(\beta)\}_{beR} \\ \{\tilde{p}(\beta)\}_{I} \end{Bmatrix} + \begin{Bmatrix} \{\tilde{s}(\beta)\}_{beR} \\ \{\tilde{s}(\beta)\}_{beI} \end{Bmatrix} \quad (4.10)$$

while equation (4.1) becomes

$$\begin{bmatrix} [K]_{feII} & [K]_{feIR} \\ [K]_{feRI} & [K]_{feRR} \end{bmatrix} \begin{Bmatrix} \{\tilde{u}(\beta)\}_{I} \\ \{\tilde{u}(\beta)\}_{feR} \end{Bmatrix} = \begin{Bmatrix} -\{\tilde{F}(\beta)\}_{I} \\ \{\tilde{F}(\beta)\}_{feR} \end{Bmatrix} \quad (4.11)$$

As indicated in equation (3.74), a transformation matrix, $[T]$, may be constructed to convert the nodal forces, $\{\tilde{F}(\beta)\}_I$, at the finite/boundary element domain interface into equivalent tractions, i.e.

$$\{\tilde{F}(\beta)\}_I = [T]\{\tilde{p}(\beta)\}_I \tag{4.12}$$

The dimension of matrix $[T]$ depends on the number of nodes at the finite/boundary element domain interface, and is in general much smaller than that of equation (4.9). When the structure is symmetric about the z-axis, $[T]$ may be constructed using half the FE/BE interface. Inserting this into equation (4.10) gives

$$\begin{bmatrix} [R]_{beRR} & [R]_{beRI} \\ [T][R]_{beIR} & [T][R]_{beII} \end{bmatrix} \begin{Bmatrix} \{\tilde{u}(\beta)\}_{beR} \\ \{\tilde{u}(\beta)\}_I \end{Bmatrix} = \begin{Bmatrix} \{\tilde{p}(\beta)\}_{beR} \\ \{\tilde{F}(\beta)\}_I \end{Bmatrix} + \begin{Bmatrix} \{\tilde{s}(\beta)\}_{beR} \\ [T]\{\tilde{s}(\beta)\}_{beI} \end{Bmatrix} \tag{4.13}$$

As indicated in this equation, the tractions on the FE/BE interface have been converted into equivalent nodal forces. By this means the possible discontinuity of tractions on the FE/BE interface does not have to be considered. Combination of equations (4.13) and (4.11), yields

$$\begin{bmatrix} [R]_{beRR} & [R]_{beRI} & 0 \\ [T][R]_{beIR} & [T][R]_{beII} + [K]_{feII} & [K]_{feIR} \\ 0 & [K]_{feRI} & [K]_{feRR} \end{bmatrix} \begin{Bmatrix} \{\tilde{u}(\beta)\}_{beR} \\ \{\tilde{u}(\beta)\}_I \\ \{\tilde{u}(\beta)\}_{feR} \end{Bmatrix} = \begin{Bmatrix} \{\tilde{p}(\beta)\}_{beR} + \{\tilde{s}(\beta)\}_{beR} \\ [T]\{\tilde{s}(\beta)\}_{beI} \\ \{\tilde{F}(\beta)\}_{feR} \end{Bmatrix} \tag{4.14}$$

This is the global equation for the whole domain.

4.3 VALIDATION

The coupled discrete wavenumber FE/BE method and the corresponding computer program have been validated by (1) calculating the response of a homogeneous half-space which is regarded as having a layered structure; (2) calculating the response of a layered ground; (3) calculating the response of a homogeneous half-space with a lined tunnel.

4.3.1 *FOR A HOMOGENEOUS HALF-SPACE WHICH IS REGARDED AS HAVING A LAYERED STRUCTURE*

Results from the coupled FE/BE model for a ground are shown in Figure 4.1. The ground consists of a layer of 2 m thickness which overlies a homogeneous half-space. The properties of the layer and those of the underlying half-space are identical to each other and are listed in Table 3.1. A unit (1 N) vertical point harmonic load of 200 Hz moving at 100 m/s in the x-direction is applied at a depth of 20 m below the ground

surface. The vertical displacements of interface (at a depth of 2 m) in the ground are displayed. For this ground, two boundary element sub-domains are introduced in the model. Both the ground surface and the interface of the two sub-domains are discretized, each with a mesh of 50 elements of one metre length over a range of 50 m (one side). In the performance of the inverse FFT, 1024 samples are used with a spacing of β equal to $0.0025\times 2\pi$ (rad/m). Also shown are the results calculated using the layered ground model [Sheng, Jones and Petyt 1999]. As can be seen, a good accuracy has been achieved.

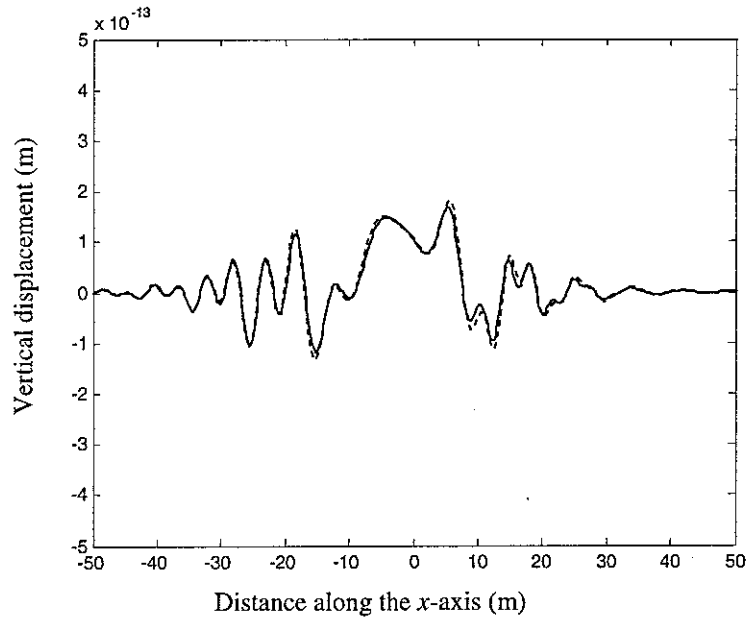

Figure 4.1.Vertical displacement along the x-axis on a plane at a depth of 2m due to a unit vertical harmonic load of 200 Hz moving at 100 m/s along the straight line ($y = 0$ m, $z = -20$ m) at a depth of 20 m. ——, calculated by the layered ground model; – – –, calculated by BEM.

4.3.2 *FOR A LAYERED GROUND*

Figures 4.2 to 4.6 present the responses of a layered ground due to a vertical harmonic load of 50 Hz which moves at 50 m/s at a depth of 20 m below the ground surface in the x-direction. The parameters of the ground are listed in Table 4.1. Two boundary element sub-domains are used to model the ground, and both the ground surface and the layer interface (one side) are approximated by 50 elements which cover a range of 50 m. The length of each element is 1 m. In other words, for each wavelength of the shear wave in the upper layer, there are about four elements.

TABLE 4.1

Parameters for a layered ground

Layer	Depth (m)	Young's modulus (10^6 Nm^{-2})	Poisson's ratio	Density (kg/m^3)	Loss factor	P-wave speed (m/s)	S-wave speed (m/s)
1	2.0	157	0.18	1517	0.1	336	210
Half space		1062.8	0.253	1759	0.1	854	491

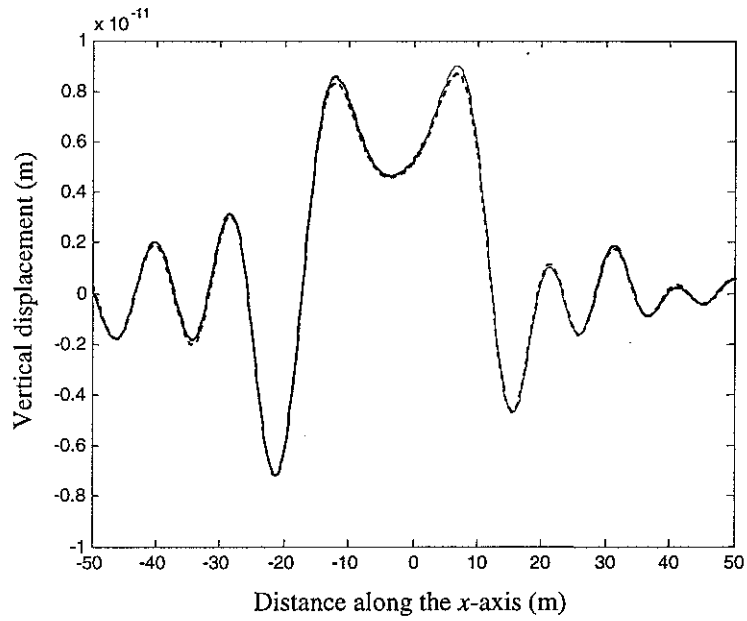

Figure 4.2. Vertical displacement along the x-axis on the ground surface due to a unit vertical harmonic load of 50 Hz moving at 50 m/s along the straight line (y = 0 m, z = -20 m) at a depth of 20 m. ——, calculated by the layered ground model; – – –, calculated by BEM.

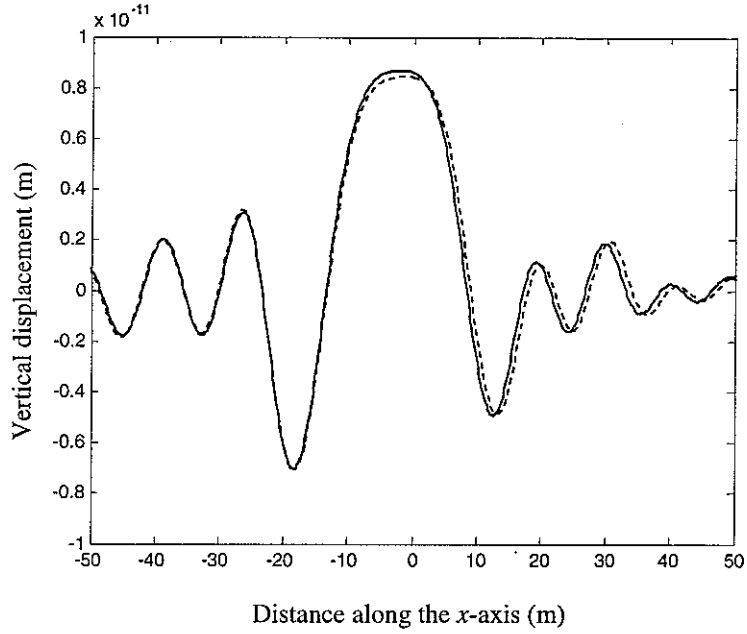

Figure 4.3. Vertical displacement along the straight line (y = 10 m) on the ground surface due to a unit vertical harmonic load of 50 Hz moving at 50 m/s along the straight line (y = 0 m, z = -20 m) at a depth of 20 m. ——, calculated by the layered ground model; – – –, calculated by BEM.

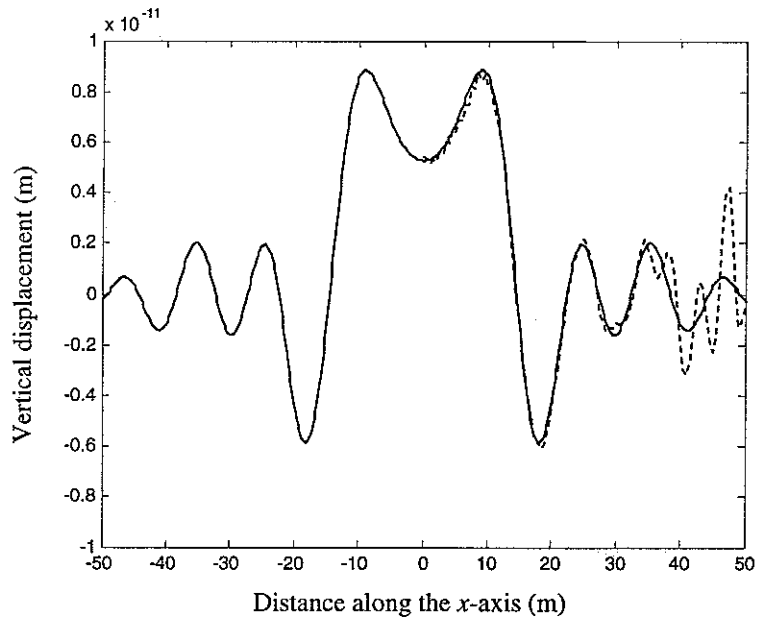

Figure 4.4. Vertical displacement along the y-axis on the ground surface due to a unit vertical harmonic load of 50 Hz moving at 50 m/s along the straight line (y = 0 m, z = -20 m) at a depth of 20 m. ——, calculated by the layered ground model; – – –, calculated by BEM.

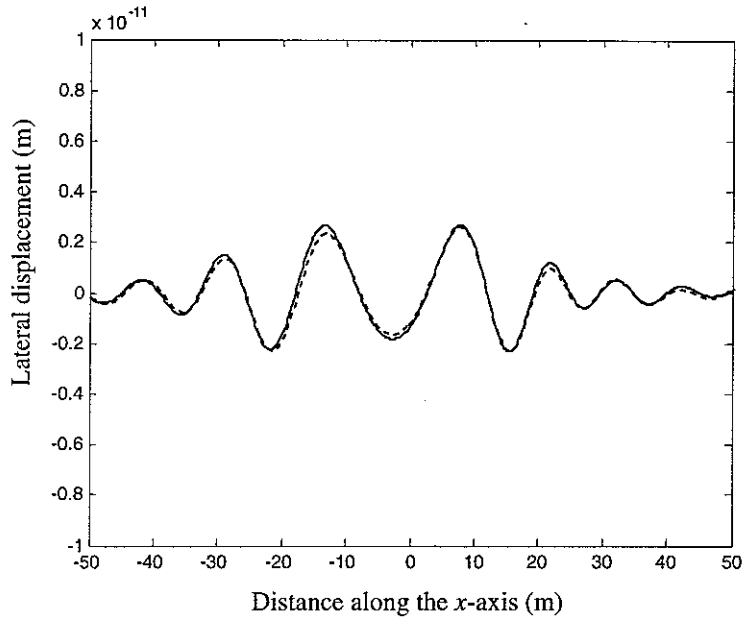

Figure 4.5. Lateral displacement along the straight line (y = 10 m) on the ground surface due to a unit vertical harmonic load of 50 Hz moving at 50 m/s along the straight line (y = 0 m, z = -20 m) at a depth of 20 m. ——, calculated by the layered ground model; – – –, calculated by BEM.

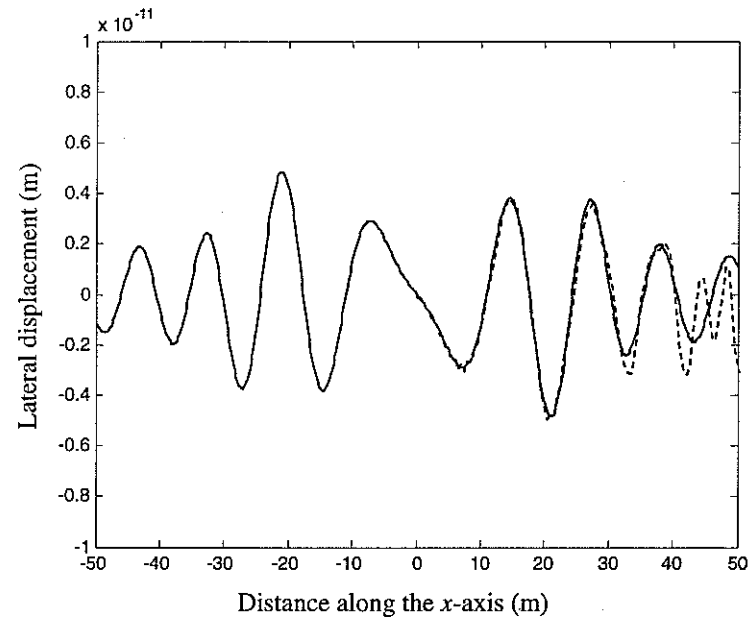

Figure 4.6. Lateral displacement along the y axis on the ground surface due to a unit vertical harmonic load of 50 Hz moving at 50 m/s along the straight line (y = 0 m, z = -20 m) at a depth of 20 m. ——, calculated by the layered ground model; – – –, calculated by BEM.

It is shown in Figures 4.4 and 4.6 that BEM solution is valid over a lateral range of 30 m. Beyond this, large error occurs due to the artificial boundary introduced at y = 50 m. This behaviour is quite different from that of a homogeneous half-space, where, as

shown in Figures 3.15 and 3.17, the BEM solution remains highly accurate over the whole BEM model, even for the homogeneous half-space including an unlined tunnel (Figure 3.19). The same observation was made in references [Jones, Thompson and Petyt 1999] and [Anderson and Jones 2001].

4.3.3 *FOR A HOMOGENEOUS HALF-SPACE WITH A LINED TUNNEL — COMPARED WITH THE FICTITIOUS FORCE METHOD*

Responses of a homogeneous half-space with a circular lined tunnel (tube) are presented in Figures 4.7 to 4.9. The parameters for the half-space are listed in Table 3.1 while those of the tunnel in Table 2.1. The lined tunnel has an average radius of 3.5 m and its axis is located at a depth of 16.5 m below the ground surface. The ground is modelled using the boundary element method while the tunnel is modelled using the finite element method. In the boundary element model 50 elements (one side) have been used with an element length equal to 1 m for the ground surface and 30 elements (one side) for the tube/soil surface. For the tunnel lining, 60 elements are distributed along its cross-section, the sizes of each being 0.2×0.37 m. In the performance of the inverse FFT, 1024 samples are used with a spacing of β equal to $0.0025\times 2\pi$ (rad/m). In addition to the results from the coupled FE/BE model, results calculated using the fictitious force method [Sheng, Jones and Thompson, 2002] are also shown in these figures for a comparison. In general, the results from these two methods are close to each other. Again, the negative effect of the edge of the BEM model is not encountered since the ground is not layered.

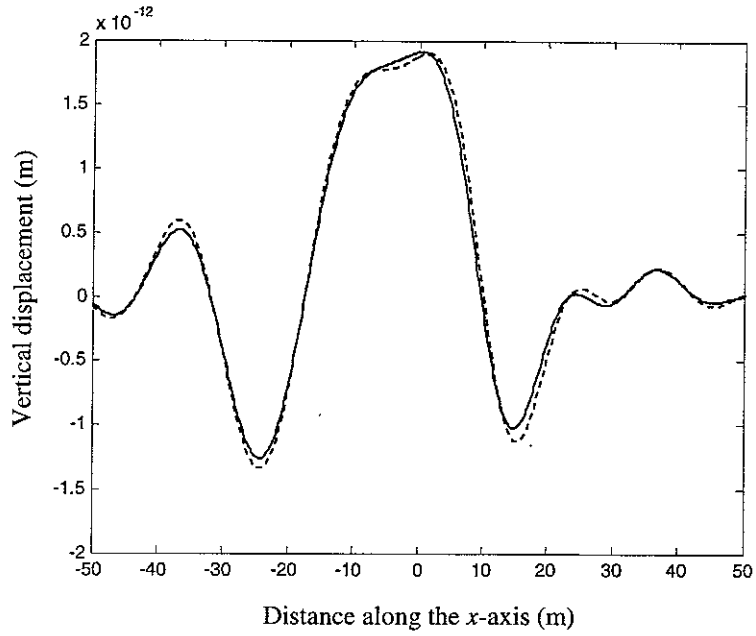

Figure 4.7. Vertical displacement along the x-axis on the ground surface due to a unit vertical harmonic load of 40 Hz moving at 100 m/s in the x-direction. The load is applied on the invert of the lined tunnel. ——, calculated by the fictitious force method; – – –, calculated by the coupled FE/BE method.

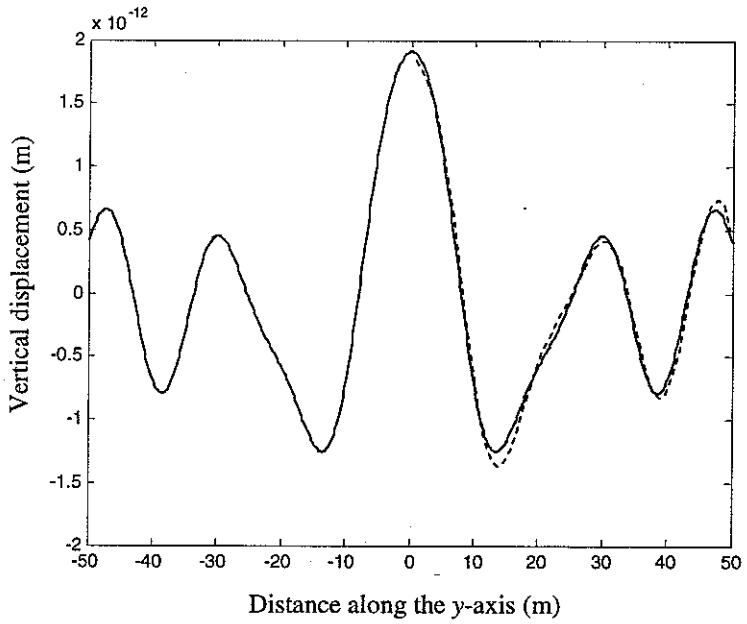

Figure 4.8. Vertical displacement along the y-axis on the ground surface due to a unit vertical harmonic load of 40 Hz moving at 100 m/s in the x-direction. The load is applied on the invert of the lined tunnel. ——, calculated by the fictitious force method; – – –, calculated by the coupled FE/BE method.

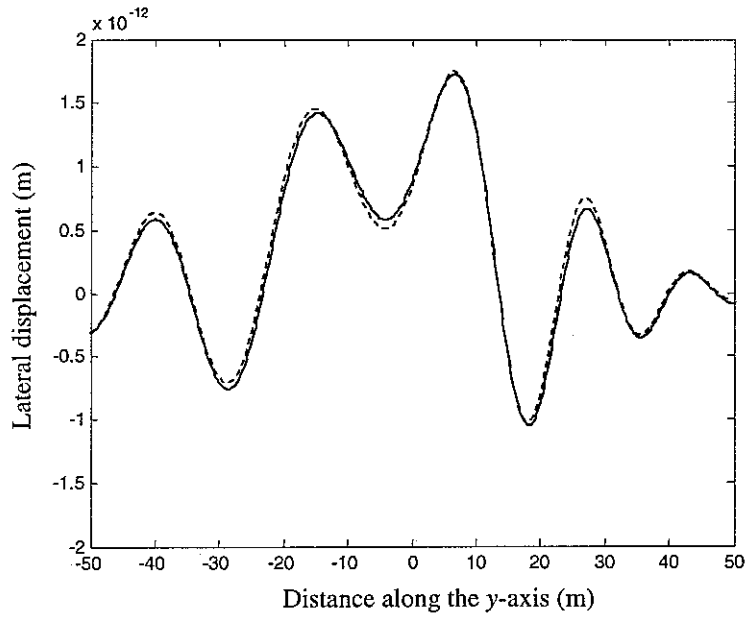

Figure 4.9. Lateral displacement along a straight line (y = 10 m) on the ground surface due to a unit vertical harmonic load of 40 Hz moving at 100 m/s in the x-direction. The load is applied on the invert of the lined tunnel. ——, calculated by the fictitious force method; – – –, calculated by the coupled FE/BE method.

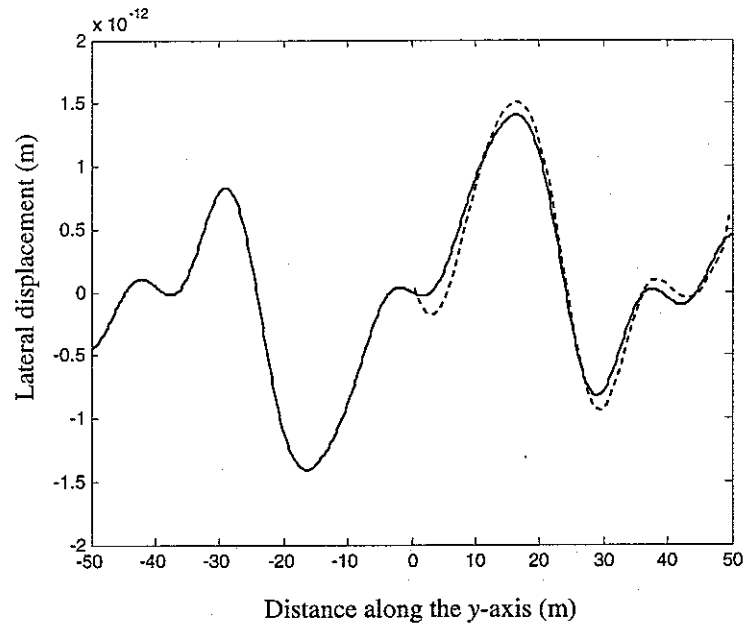

Figure 4.10. Lateral displacement along the y-axis on the ground surface due to a unit vertical harmonic load of 40 Hz moving at 100 m/s in the x-direction. The load is applied on the invert of the lined tunnel. ——, calculated by the fictitious force method; – – –, calculated by the coupled FE/BE method.

5. CONCLUSIONS

The theory for a multi-domain FE/BE scheme has been formulated in the frequency-wavenumber domain for the prediction of responses of structures which are homogeneous in one direction and subject to harmonic loads moving uniformly in that direction. The cross-section of the sub-domains may be either open or closed and may be arbitrarily shaped. Thus this scheme is useful for the analysis of many structure-soil interaction problems involving stationary or moving harmonic excitations, such as ground vibration generated by underground trains. Example calculations and comparisons with other methods show this scheme works very well. To achieve an acceptable accuracy for a boundary element domain, more than three elements should be implemented in each wavelength. For a coupled FE/BE domain in particular, more tests should be conducted to identify the relationship between the fineness of mesh and frequency.

REFERENCE

Andersen, L. and Jones, C. J. C. 2001. *ISVR Technical Memorandum No. 867, University of Southampton.* Three-dimensional elastodynamics analysis using multiple boundary element domains.

Andersen, L. and Jones, C. J. C. 2001. *ISVR Technical Memorandum No. 868, University of Southampton.* BEASTS-A computer program for Boundary Element Analysis of Soil and Three-dimensional Structures.

Aubry, D., Clouteau, D. and Bonnet, G. 1994 *Wave Propagation and Reduction of Vibrations*, Chouw and Schmid edition, Berg-Verlag, Bochum, 109-121. Modelling of wave propagation due to fixed or mobile dynamic sources.

Dominguez, J. 1993 Boundary Elements in Dynamics. *Elsevier Applied Science.*

Eason, G., Fulton, J. and Sneddon, I. N. 1955/1956 *Phil. Trans. Roy. Soc. London* **248** (A955), 575-607. The generation of waves in an infinite elastic solid by variable body forces.

Forrest, J. A. 1999 *PhD Dissertation, Cambridge University.* Modelling of the ground vibration from underground railways.

Gavric, L. 1995 *Journal of Sound and Vibration*, **185**(3), 531-543. Computation of propagative waves in free rail using a finite element technique.

Gavric, L. 1994 *Journal of Sound and Vibration*, **173**(1), 113-124. Finite element computation of dispersion properties of thin-walled waveguides.

Grootenhuis, P. 1977 *Journal of Sound and Vibration* **51**(3), 443-448. Floating track slab isolation for railway.

Johnston, P. R. and Johnston, B. M. 2002 *Communications in Numerical Methods in Engineering*, **18**, 189-194. A simple device to improve the accuracy of evaluating weakly singular boundary element integrals.

Jones, C. J. C., Thompson, D. J. and Petyt, M. 1999 *ISVR Technical Memorandum No. 844, University of Southampton.* Ground-borne vibration and noise from trains:

Elastodynamic analysis using the combined boundary element and finite element methods.

Leissa, A. W., 1973 Vibration of Shells. National Aeronautics and Space Administration.

Mead, D. J. 1973 *Journal of Sound and Vibration*, **27**, 235-260. A general theory of harmonic wave propagation in linear periodic systems with multiple coupling.

Mustoe, G. G. W. 1980 *A Combination of the Finite Element and Boundary Element Integral Procedures*, PhD thesis, Swansea University, UK.

Petyt, M. 1990 *Introduction to Finite Element Vibration Analysis.* Cambridge University Press.

Shah, A. H., Zhuang, W., Popplewell, N. and Rogers, J. B. C. 2001 *Transaction of the ASME Journal of Vibration and Acoustics*, **123**, 376-382. Guided waves in thin-walled structural members.

Sheng, X., Jones, C. J. C. and Thompson, D. J. 2002 *University of Southampton, Institute of Sound and Vibration Research, Technical Memorandum* 890. Ground vibration generated by a harmonic load moving in a circular tunnel in a layered ground.

Sheng, X., Jones, C. J. C. and Thompson, D. J. 2002 *University of Southampton, Institute of Sound and Vibration Research, Technical Memorandum* 885. Moving Green's functions for a layered circular cylinder of infinite length.

Sheng, X. 2001 *PhD Dissertation, University of Southampton.* Ground vibrations generated from trains.

Sheng, X., Jones, C. J. C. and Petyt, M.1999 *University of Southampton, Institute of Sound and Vibration Research, Technical Memorandum* 837. The Fourier transformed stationary and moving flexibility matrices of a layered ground.

Singh, K. M. and Tanaka, M. 2001 *International Journal for Numerical Methods in Engineering,* **50**, 2007-2030. On non-linear transformations for accurate numerical evaluation of weakly singular boundary integrals.

Tadeu, A.J.B. and Kausel, E. *2000 Journal of Engineering Mechanics* **126**(10), 1093-1097. Green's functions for two-and-a-half-dimensional elastodynamic problems.

Takemiya, H. and Yuasa, S. 1999 *Structural Dynamics-EURODYN'99*, Balkema, Rotterdam, 821-826. Lineside ground vibration induced by high-speed trains and mitigation measure WIB.

Thompson, D. J. 1993 *Journal of Sound and Vibration*, **161**(3), 421-446. Wheel-rail noise generation, Part III: Rail vibration.

Tullberg, O. and Bolteus, L. 1982 *Boundary Element Methods in Engineering*, Ed. C. A. Brebbia, 625-635. A critical study of different boundary element stiffness matrices.